

MaxBCG: A Red Sequence Galaxy Cluster Finder

Benjamin P. Koester¹,

bkoester@umich.edu

Timothy A. McKay¹,

tamckay@umich.edu

James Annis², Risa H. Wechsler^{3,4,5}, August E. Evrard¹,
Eduardo Rozo^{3,6}, Lindsey Bleem⁶, Erin S. Sheldon⁷, David Johnston⁸

ABSTRACT

Measurements of galaxy cluster abundances, clustering properties, and mass-to-light ratios in current and future surveys can provide important cosmological constraints. Digital wide-field imaging surveys, the recently-demonstrated fidelity of red-sequence cluster detection techniques, and a new generation of realistic mock galaxy surveys provide the means for construction of large, cosmologically-interesting cluster samples, whose selection and properties can be understood in unprecedented depth. We present the details of the “maxBCG” algorithm, a cluster-detection technique tailored to multi-band CCD-imaging data. MaxBCG primarily relies on an observational cornerstone of massive galaxy clusters: they are marked by an overdensity of bright, uniformly red galaxies. This detection scheme also exploits classical brightest cluster galaxies (BCGs), which are often found at the center of these same massive clusters. We study the algorithm herein through its performance on large, realistic, mock galaxy catalogs,

¹Department of Physics, University of Michigan, Ann Arbor, MI 48104

²NASA/Fermilab Astrophysics Center, Fermi National Accelerator Laboratory, Batavia, IL

³Kavli Institute for Cosmological Physics, The University of Chicago, Chicago, IL 60637

⁴Department of Astronomy and Astrophysics and Enrico Fermi Institute, The University of Chicago, Chicago, IL 60637

⁵Hubble Fellow

⁶Department of Physics, The University of Chicago, Chicago, IL 60637

⁷Center for Cosmology and Particle Physics and Department of Physics, New York University, New York, NY 10003

⁸Jet Propulsion Laboratory, Caltech, Pasadena, CA 91109

which reveal that it is $> 90\%$ pure for clusters at $0.1 < z < 0.3$ with 10 or more red galaxies, and $> 90\%$ complete for halos at $0.1 < z < 0.3$ with masses of $> 2 \times 10^{14} h^{-1} M_{\odot}$. MaxBCG is able to approximately recover the underlying halo abundance function, and assign cluster richnesses strongly coupled to the underlying halo properties. The same tests indicate that maxBCG rarely fragments halos, occasionally overmerges line-of-sight neighboring ($\simeq 10 h^{-1}$ Mpc) halos, and overestimates the intrinsic halo red sequence galaxy population by no more than 20%. This study concludes with a discussion of considerations for cosmological measurements with such catalogs, including modeling the selection function, the role of photometric errors, the possible cosmological dependence of richness measurements, and fair cluster selection across broad redshift ranges employing multiple bandpasses.

Subject headings: galaxies: clusters — cosmology: observations — methods: data analysis

1. Introduction

Clusters of galaxies are the largest bound objects in the Universe. They are the likely observational counterparts of dark matter halos, whose masses, abundance, and distribution are sensitive probes of cosmology. Dark matter dominates their matter content, with baryons forming no more than $\simeq 15\%$ of the total mass (Voit 2005, and references therein). The baryonic component is comprised of stars bound to constituent galaxies, stars that make up the intra-cluster light (Zwicky 1951; Gonzalez et al. 2005; Krick et al. 2006), and a hot intra-cluster medium which accounts for $\simeq 7/8$ of the baryons (David et al. 1995; Evrard 1997; Allen et al. 2002). In addition to fueling stars, the gas component is responsible for X-ray emission (Sarazin 1986; Rosati et al. 2002) and Sunyaev-Zeldovich decrements (Carlstrom et al. 2002), all of which make possible the baryonic detection of dark matter halos.

In cosmological measurements, the high end of the halo mass function is the most observationally accessible. In this regime, cluster abundances are most sensitive to changes in the proper distance at low redshift. By $z \gtrsim 1$, abundances become more sensitive to the growth function (Haiman et al. 2001; Levine et al. 2002; Battye & Weller 2003). This sensitivity has motivated numerous X-ray and optical searches for the most massive clusters across a range of redshifts. Observations provide constraints on the abundance of clusters as a function of observables such as X-ray luminosity or optical richness. Extracting cosmological constraints from these observations requires a good understanding of the relationship between

these observables and the underlying cluster mass.

Among the various cluster detection schemes, optical imaging catalogs enjoyed the earliest successes, targeting the high S/N end of the abundance function across a range of redshifts. These began with the early photographic plate surveys of Abell (Abell 1958; Abell et al. 1989) and Zwicky (Zwicky et al. 1968) and have since moved to digitized plate catalogs (Lumsden et al. 1992; Dalton et al. 1997; Gal et al. 2000) and CCD-imaging catalogs (Postman et al. 1996; Annis et al. 1999; Olsen et al. 1999; Lobo et al. 2000; Goto et al. 2002; Gladders & Yee 2005). During the 1980’s, large spectroscopic catalogs were also generated, drawing from a host of redshift surveys including the CfA redshift survey, (Huchra & Geller 1982, and many others), the Nearby Galaxies Catalog (Tully 1987), the ESO Slice Project (Ramella et al. 1999), the Las Campanas Redshift Survey (Tucker et al. 2000), the Nearby Optical Galaxy Sample (Giuricin et al. 2000), the Southern Sky Redshift Survey (Ramella et al. 2002), the 2df redshift survey (Merchán & Zandivarez 2002; Eke et al. 2004; Yang et al. 2005), the Sloan Digital Sky Survey (Miller et al. 2005; Berlind et al. 2006), and DEEP2 (Gerke et al. 2005).

At about the same time, space-based X-ray telescopes became an invaluable tool for cluster science, detecting hundreds of X-ray luminous clusters in flux limited surveys (Schwartz 1978; Gioia et al. 1990; Ebeling et al. 1998; Böhringer et al. 2001, 2004). Individual clusters have been detected in this way out to $z \simeq 1.4$ (Mullis et al. 2005; Brodwin et al. 2005). More recently, the Sunyaev-Zeldovich Effect has been cited as a powerful means for cluster detection (Carlstrom et al. 2002). Imminent ground-based Sunyaev-Zeldovich surveys promise nearly redshift-independent detections of a range of halos (Ruhl et al. 2004; Loh et al. 2005).

While finding massive clusters has become more routine, returning robust cosmological constraints has proven challenging. For any method of detecting clusters, robust cosmological constraints are impossible without a reliable estimate of the absolute calibration of and scatter in the observable–mass relation. Scatter can be due to both the stochastic nature of the physics that relates the observables to mass, and to noise in the measurements themselves. Because the abundance function drops precipitously with increasing mass, any attempted selection of dark matter halos imposed by a cut on an observable in this high-mass regime scatters systems asymmetrically above and below this cut, a selection effect known as Eddington bias (Eddington 1913). In the exponential tail of the distribution, the number of objects scattered up across the threshold in the observable considerably exceeds the number scattered down, and depending on the size of the scatter, this difference can be comparable to the sample size itself. (e.g., Lima & Hu 2005).

The quality of the cosmological constraints from any measurement of cluster abundances will depend on the amount of scatter between the observable and halo mass, on the dynamic

range of masses probed, and on how well the mass–observable relation can be calibrated. Thus interpretation of these abundance measurements typically requires complex modeling strategies (Ikebe et al. 2002; Holder et al. 2000; Levine et al. 2002; Battye & Weller 2003) or self-calibration techniques (Majumdar & Mohr 2003, 2004; Lima & Hu 2005) to calibrate them and to account for the selection biases incurred by the scatter in the mass-observable relation. In addition, self-calibration techniques may be more challenging than previously expected if halo clustering depends on properties other than mass (Wechsler et al. 2006b).

Despite their challenges, optically-selected cluster catalogs offer many advantages over other methods. Optical surveys are generally able to detect individual galaxies at high S/N to high redshift and in wide fields. This has enabled spectroscopic surveys to identify halos at the group scale. Imaging catalogs can in principle do the same, over a substantially larger redshift range, if they can limit the degrading effects of projection. By contrast, X-ray surveys are relatively insensitive to projection issues (Ebeling et al. 1998; Böhringer et al. 2000) and can be used to detect intermediate-mass groups. Unfortunately the relatively low X-ray luminosity of groups limits detection to the most luminous or low redshift objects.

In addition to the obvious advantage of more bang for the buck if photometric surveys can be used to identify clusters robustly — indeed, such surveys are often done primarily for other reasons, such as the measurement of the galaxy power spectrum — there are substantial advantages to identifying systems farther down the abundance function. First, cosmological constraints are improved when one can measure the mass function over a larger dynamic range: e.g., the *difference* in the abundance of low mass to high mass systems can constrain the normalization of the power spectrum with less degeneracy than the pure abundance of the highest mass systems. Second, the effect that scatter has on weakening constraints are somewhat mitigated when one can identify systems farther down the abundance function, where the mass function is shallower.

The other strong advantage of optical surveys over other methods is the vast amount of additional data available on the clusters, that can both contribute to mass calibration and that can inform our understanding of galaxy evolution. In addition to measurements of cluster clustering (e.g. Gonzalez et al. 2002) that are possible with other types of selection, the galaxies used to identify the clusters can also be used for weak lensing measurements (Sheldon et al. 2001, 2006), and for velocity measurements if some or all of the galaxies have spectra (e.g., Yang et al. 2005; McKay et al. 2006). They can also be used to measure the luminosity function and profiles of galaxy clusters (Hansen et al. 2005; Popesso et al. 2005), and the cluster mass-to-light-ratio (Tinker et al. 2005; Popesso et al. 2006), which can improve cosmological constraints when combined with galaxy clustering measurements (van den Bosch et al. 2003).

As we will show, in imaging surveys, cluster catalogs that span a broad range of masses and redshifts are a possibility. Minimizing projection is the primary driver behind modern cluster and group-finding algorithms. In recent years, imaging-based techniques have matured with the construction of galaxy catalogs from surveys such as the Digitized Second Palomar Observatory Sky Survey (DPOSS; Djorgovski et al. 1999), the Palomar Distant Cluster Survey (PDCS; Postman et al. 1996), the Red-Sequence Cluster Survey (RCS; Gladders & Yee 2005), and the Sloan Digital Sky Survey (SDSS; York et al. 2000) to name a few. Automated efforts were initiated in photographic plates, beginning with counts-in-cells techniques (Couch et al. 1991; Lidman & Peterson 1996) and adaptive kernel estimators (Gal et al. 2000, 2003). Around the same time the powerful matched-filter (Postman et al. 1996) and adaptive matched filter (Kepner et al. 1999) codes were developed for use on the new CCD imaging. The adaptive kernel method of Gal et al. (2000) was among the first to employ color cuts conducive to cluster galaxy selection in their codes. The Red-Sequence method (Gladders & Yee 2000) was the first to explicitly use color selection of red-sequence galaxies as the primary lever arm for cluster detection. The cut-and-enhance (Goto et al. 2002) and the spectroscopic C4 algorithms (Miller et al. 2005) generalized this notion of color uniformity to clustering in any color.

The guiding principles usually invoked in the appraisal of these cluster finders are that the algorithm must be automated and objective, should impose minimal constraints on cluster properties, have a well-understood selection function, and should provide physical properties of the clusters, such as redshift, luminosity, and richness (Gal et al. 2003; Gal 2006). The preceding algorithms address these points with varying degrees of success, and primarily concern themselves with the optically-richest systems. Since cosmology with clusters of galaxies is an integral component of many current and future surveys, cluster-finding algorithms that exploit the full power of modern imaging surveys will become increasingly important as well. In addition to uncovering the most massive halos, it is desirable that they should also produce cluster catalogs that extend down the mass function, to measure the mass function over the largest possible dynamic range.

Evidence from studies of galaxy environments suggest a means by which to accomplish this. Galaxies in dense environments preferentially exhibit both early-type morphologies (Hashimoto & Oemler 1999; Goto et al. 2003; Kuehn & Ryden 2005) and red colors (Balogh et al. 2004; Hogg et al. 2004; Tanaka et al. 2004). Indeed, Weinmann et al. (2006, and references therein) confirm that the red fraction in clusters increases with increasing halo mass and luminosity, and decreasing halo-centric radius. Thus, the presence of a nascent red galaxy population in lower mass, lower richness halos, although less evolved than the red galaxy population of massive clusters, provides the opportunity to extend cluster detection to lower mass scales.

In this work, we present “maxBCG”, an optical cluster-finding algorithm adapted specifically to wide-field, multi-band digital imaging surveys, such as the Sloan Digital Sky Survey (SDSS). This algorithm takes advantage of observational cornerstones of cluster galaxies: they are typically the brightest galaxies at a given redshift; their brightest members share very similar colors; and they are spatially clustered. As we will show, these properties alone are sufficient to robustly select and center the richest clusters, while the power of the red-sequence takes over at lower richness to select group-sized objects. Combining these factors in an algorithm, and running it on surveys with the size and quality of the SDSS imaging enables the generation of immense, high-quality cluster catalogs whose selection function can be quantitatively determined. Between $0.1 < z < 0.3$, maxBCG can reliably identify objects with > 10 red galaxies, and masses of $\sim 2 \times 10^{14} M_{\odot}$ in a volume limited way.

Section 2 of this paper contains an outline of the maxBCG algorithm, and the details of its components. The execution of the algorithm is covered in §3, followed by study of the selection function and performance of the algorithm in mock galaxy catalogs in §4. A discussion and summary conclude the paper. Throughout this paper, we assume $\Omega_m = 0.3, \Omega_{\Lambda} = 0.7$ and $h = 1$. A companion paper, Koester et al. (2006), presents a catalog of 13,823 clusters identified using this method from SDSS data, over the redshift range $0.1 < z < 0.3$.

2. Algorithm

2.1. Outline

We introduce the maxBCG algorithm, a new cluster detection technique which exploits three primary features of galaxy clusters. The first is the obvious spatial clustering of galaxies in clusters, which falls off as $\sim 1/r$ projected in 2 dimensions (Section 2.3). The second is that the most luminous cluster galaxies inhabit a tight sequence in the color-magnitude diagram (CMD), the so-called “E/S0 ridgeline”. The galaxies in the E/S0 ridgeline have very uniform colors, and are among the reddest, brightest, and rarest galaxies at a given redshift. Because of the strong 4000 Å break in their rest-frame spectra, their color is tightly correlated with redshift, so that color measurements have the additional advantage that they provide accurate redshift estimates.

The last feature is that there often exists a unique brightest cluster galaxy (BCG) that resides in the E/S0 ridgeline, is typically coincident with the center of the galaxy distribution, and is nearly at rest relative to the halo center. BCGs in rich clusters usually take the form of giant elliptical galaxies, so large that they are only found at the centers of galaxy clusters.

Thus they provide important additional information about cluster locations and redshifts.

These features are folded into a likelihood function which is redshift-dependent. Individual objects in an input photometric galaxy catalog are evaluated at an array of redshifts with this composite function, to assess the likelihood that they are BCGs living in an overdense environment consisting of galaxies with a small dispersion in color. An outline of algorithm is as follows:

1. Using the likelihood function, each object in an input galaxy catalog is tested at an array of redshifts for the likelihood that it is a cluster center.
2. Each object is assigned the redshift which maximizes this likelihood function.
3. The objects are ranked by these maximum likelihoods.
4. The object with the highest likelihood in the list becomes the first cluster center. All other objects within $z = \pm 0.02$ (the typical σ_z on a red galaxy), a scaled radius r_{200} , and lower maximum likelihood are removed from the list of potential centers.
5. The next object in the list is handled similarly, and the process is continued, flagging other potential cluster centers within that object's neighborhood which have lower likelihoods.
6. All unflagged objects at the end of this percolation are kept, and are taken as BCGs identifying clusters in the final cluster list.

As a consequence of this method, each cluster gets a photometric redshift, the redshift which maximizes its likelihood of being a cluster center. During the process, the number of galaxies within $1h^{-1}$ Mpc, within $\pm 2\sigma$ of the E/S0 ridgeline, and brighter than some minimum luminosity, L_{min} (see section 2.5), and dimmer than the BCG is recorded as N_{gals} , an initial richness estimate. A scaled richness estimate, N_{gals}^{r200} , is also generated. The only difference from N_{gals} is that instead of using a fixed aperture, it counts objects within r_{200} of the BCG, where $r_{200} = 0.156N_{gals}^{0.6}h^{-1}$ Mpc (Hansen et al. 2005).

In the following, the components of the likelihood function encoding these properties are outlined and the overall likelihood function is described. The section concludes with a description of the input galaxy catalog. Along the way we justify the choices made in design of the algorithm.

2.2. Likelihood Framework

The general strategy for finding clusters in maxBCG is to maximize the likelihood that a galaxy resides at the center of a cluster by varying the redshift. This is a two-part likelihood function. One part checks a galaxy for its similarity to a BCG, and the other part measures the match of a galaxy’s environment to the E/S0 ridgeline. In what follows, we build the components of the likelihood:

$$\mathcal{L}_{tot}(z) = \mathcal{L}_{BCG}(z)\mathcal{L}_R(z) \quad (1)$$

where \mathcal{L}_{BCG} and \mathcal{L}_R are the BCG and ridgeline likelihoods. The algorithm proceeds by evaluating this full likelihood function for the whole galaxy density field and labeling peaks in the field.

2.3. Ridgeline Likelihood

The ridgeline likelihood is broken up into spatial and color filters, which are folded into a matched-filter likelihood. Each component contains parameters that are driven observationally, such as the width of the E/S0 ridgeline, or theoretically, such as the NFW density (Navarro et al. 1996) profile.

2.3.1. Spatial Filter

N-body simulations and studies of galaxy distributions in rich clusters (e.g., on early versions of this algorithm, Hansen et al. 2005) have shown that both the distribution of dark matter around dark matter halos and the distribution of galaxies around cluster centers can be well-modeled by an NFW profile. In three dimensions,

$$\rho(r) = \delta_c \rho_c \frac{1}{(r/r_s)(1 + r/r_s)^2}, \quad (2)$$

where $r_s = r_{200}/c$ is a scale radius, c and δ_c are dimensionless parameters, and ρ_c is the critical density. With $x = r/r_s$, Bartelmann (1996) has shown that this can be written as a surface density:

$$\Sigma(x) = \frac{2\rho_s r_s}{x^2 - 1} f(x) \quad (3)$$

with

$$f(x) = \begin{cases} 1 - \frac{2}{\sqrt{x^2-1}} \tan^{-1} \sqrt{\frac{x-1}{x+1}} & x > 1 \\ 1 - \frac{2}{\sqrt{1-x^2}} \tanh^{-1} \sqrt{\frac{1-x}{x+1}} & x < 1 \\ 0 & x = 1 \\ 0 & x > 20 \end{cases} \quad (4)$$

Because $f(x)$ diverges at small x , and because this assumption is shakier at small radii, the profile is truncated at $x = 0.667$, or $r = 100h^{-1}$ kpc (see below). Objects near the center are given large weights, and those far away are strongly down-weighted. This model allows for a variable scale radius, r_s that could be additionally maximized to provide an optimal size for each cluster. We choose a fixed $r_s = 150$ kpc in this implementation. This quantity is normalized to 1 by integrating the area over $0.0 < r < 3h^{-1}$ Mpc ($0.0 < x < 20$). Tests show that varying r_s between 100 kpc and $1h^{-1}$ Mpc only has a very marginal influence on the overall abundance function or the algorithm selection function. In general, and in accordance with other authors (Lubin & Postman 1996; Gladders & Yee 2000), we find that the exact parameters of the radial likelihood function have only a minimal effect on the performance. Only extremes, such as top-hat spatial filters that have sharp edges, strongly influence the performance.

2.3.2. Color Filter

Investigations of rich clusters indicate the presence of a universal red-sequence, extending from the nearby Coma and Virgo clusters (Bower et al. 1992), through intermediate redshifts (Smail et al. 1998; Barrientos 1999), and out to redshifts as high as $z \sim 1.4$ (Mullis et al. 2005; Eisenhardt et al. 2005). This population of galaxies dominates the bright end of the cluster luminosity function (Sandage et al. 1985; Barger et al. 1998) and consists of E and S0 galaxies objects with a narrow scatter in color, hence its designation as the “E/S0 ridgeline” (Visvanathan & Sandage 1977; Annis et al. 1999, Figure 1). This tight sequence is due to the presence of the uniformly old underlying stellar populations in these galaxies, resulting from passive evolution and minimal star formation. In Coma and Virgo, the stellar component has most likely been in place for at least 2 Gyr (Bower et al. 1992). For a review of the red sequence in galaxy clusters, see Gladders & Yee (2000) and references therein.

The red sequence is not limited to galaxy clusters. It persists smoothly down to the lower density environments harbored in groups (Postman & Geller 1984; Zabludoff & Mulchaey 1998; Tran et al. 2001). Transformation of a field spiral into a red-sequence elliptical has been hypothesized to occur in two steps (e.g., Weinmann et al. 2006): 1) mergers between spiral galaxies in low velocity groups create ellipticals (Toomre & Toomre 1972), which in turn 2)

are stripped of their hot gas through processes such as ram pressure stripping and galaxy harassment, effectively truncating star formation (Larson et al. 1980; Balogh et al. 2000). This picture has been supplemented by recent simulations which implicate active galactic nucleus (AGN) feedback in truncating star-formation (e.g., Croton et al. 2006). Depending on the state of the evolution of the group and the possible presence of AGN, the E/S0 ridgeline may be ill-defined in a given group. However, the presence of red-sequence galaxies is ubiquitous in higher mass groups, and extends substantially farther down the richness function than any properties that depend on cluster gas properties.

Motivated by the location of the 4000 Å break and the luminous red galaxy (LRG) cuts outlined by Eisenstein et al. (2001), we employ cuts in SDSS $g - r$ and $r - i$ in our search (Section 3), which depend on the color-redshift relation of the E/S0 ridgeline. First, we measured the width of the ridgeline using stacked Abell clusters at $z \simeq 0.1$ in the SDSS spectroscopic survey, and fit a line to the color-magnitude diagrams, as there is a small tilt. We then projected the distribution along the line. The resulting color distributions are well-fit by Gaussians with widths of 0.05 and 0.06 in $g - r$ and $r - i$, in agreement with a range of studies (Bower et al. 1992; Smail et al. 1998; López-Cruz et al. 2004; Barrientos et al. 2004); since the color errors are small ($\simeq 0.005$ mag) for this bright sample ($r \lesssim 17.7$), most of the width is intrinsic to the ridgeline. This information is folded into \mathcal{L}_R for some color $j - k$ using a normalized function G_{j-k} , of the following form:

$$G_{j-k}(z) = \frac{1}{\sqrt{2\pi}\sigma} \exp \frac{(x_{j-k} - \bar{x}(z))^2}{2\sigma^2} \quad (5)$$

where x_{j-k} is the color of some galaxy being tested, $\bar{x}(z)$ is the predicted E/S0 ridgeline color at some redshift (see below) and the width, σ , is determined according to

$$\sigma = \sqrt{\sigma_{j-k}^2 + (\sigma_{j-k}^r)^2} \quad (6)$$

Here, σ_{j-k} is the error in the measured color of an individual galaxy and σ_{j-k}^r is the intrinsic width of the E/S0 ridgeline, 0.05 for $g - r$ and 0.06 for $r - i$. The ridgeline width is taken to be constant with both redshift and richness, a reasonable approximation for the redshift range considered here. It is clear that this function will peak in the field of a rich cluster when the right redshift-color combination is tested, and that the peak will be strong for galaxies with well-measured colors and for clusters with especially tight E/S0 ridgelines.

One feature of this prescription is that the photometric error, σ_{j-k} , is folded into the cluster detection process. Galaxies with poorer color measurements are able to contribute to ridgelines at a wider range of redshifts, albeit at a suppressed level because of the breadth of G_{j-k} . Those with good color measurements have a very narrow, highly peaked G_{j-k} , such

that they make a very strong contribution to the ridgeline at the right redshift, and a vanishingly small contribution to ridgelines at other nearby redshifts. The input of photometric errors to cluster detection is somewhat similar to that in Gladders & Yee (2000), where the color slices are defined according to the typical photometric error and the intrinsic ridgeline width. For comparison, Goto et al. (2002) use photometric error estimates to exclude galaxies from the cluster detection process whose color errors are larger than the expected ridgeline width. Kim et al. (2002) and Gal et al. (2000) do not use the photometric error explicitly in cluster detection.

As noted by Gladders & Yee (2000), the fiducial color–redshift model, $\bar{x}(z)$, does not need to be perfect to find clusters; clustering in color requires little knowledge of redshift. However, accurate color–redshift relations are certainly helpful in providing accurate photometric redshifts. This is a very reasonable demand, as the strong 4000Å break feature in red-sequence galaxies makes $g - r$ an effective indicator of redshift. This feature enables red-sequence algorithms to deliver accurate photometric redshifts without spectra. The accuracy of the photometric redshifts is borne out in the accompanying maxBCG catalog paper (Koester et al. 2006), where the photometric redshift errors are shown to be $\sigma_z < 0.015$ for clusters with $N_{gals}^{r200} > 10$ and with $0.1 < z < 0.3$. For comparison, in the SDSS, the method of Goto et al. (2002) also returns photometric redshift errors of $\sigma_z = 0.0147$ over a similar redshift range, while the hybrid-matched filter of Kim et al. (2002) has errors that range from $\sigma_z = 0.007$ to 0.02. Outside the SDSS, the digitized NSC (Gal et al. 2003) survey reaches σ_z as low as 0.033, while the RCS (Gladders & Yee 2005) estimate $\sigma_z = 0.05$ over $0.2 < z < 1.0$.

In maxBCG, the determination of $\bar{x}(z)$ is driven observationally, by the SDSS LRGs (Eisenstein et al. 2001) whose colors and redshifts serve as a template. An advantage of using the LRGs is the fact that they provide observationally-determined colors and redshifts of the early-type galaxies that we expect to be in dense environments. A drawback is that the standard LRG color–magnitude selection criteria are only valid for $z > 0.15$, so that LRGs outside this range must be selected by alternate means. We handle this shortcoming by using a combination of spectroscopic classification (`eclass` < 0) and morphology (`fracDevr` > 0.8) (Stoughton et al. 2002; Bernardi et al. 2005) to extract luminous early-type galaxies below $z = 0.15$ from the SDSS full spectroscopic sample (Adelman-McCarthy et al. 2006). The $g - r$ and $r - i$ colors of these spectroscopically-identified objects were used to predict the ridgeline colors of $z < 0.15$ clusters. A fiducial version of the cluster finder was then run, and spectroscopically-identified cluster members were used to create a refined prediction of the color–redshift relation at $z < 0.15$.

Beyond $z = 0.15$, where the standard LRG selection is robust, and clusters with multiple

member spectra are less common, the LRG colors were used to select the initial cluster galaxies. Their colors were then used to calibrate the color–redshift relation. The resulting piecewise-defined function for determination of the ridgeline $g-r$ color vs. redshift is shown in Figure 2. A similar relation exists for $r-i$. The combined $g-r$ and $r-i$ models constructed in this way are at the heart of the ridgeline component of the likelihood function, as well as the photometric redshifts provided by this algorithm.

For comparison, the LRG $g-r$ colors are shown in Figure 2, as shown in Table 1 of Eisenstein et al. (2001). The upper and lower short dashed lines are the $g-r$ colors predicted from their Pegase simulations for passive (upper) and star-forming (lower) dotted lines. The LRG cuts in the SDSS are designed to select the brightest $\gtrsim 3L_*$ red galaxies, which should also be the reddest. The upper short-dashed line indeed falls on the red end of the cluster galaxy colors at each redshift, and the star-forming model forms a sort of lower bound for the cluster members, so the cluster colors (and our model) compare quite well with the LRG sample.

2.3.3. Constructing the Ridgeline Likelihood

The general framework for developing \mathcal{L}_R is identical to that derived by Postman et al. (1996). The following reviews this process. The application of this formalism to our filters is valid as long as the assumptions about the Gaussian character of the galaxy number counts in a given angular aperture hold. Even when this begins to fail, the efficacy of the red sequence and the fact that the likelihoods are used as a ranking tools (§3) and not as absolute assignments of cluster significance allows us to use this method of identification for relatively low mass groups.

The framework is constructed by first writing down the cluster likelihood:

$$\mathcal{L}_R \sim \frac{1}{\sigma} \exp \frac{[b(c) + \Lambda_N M(r, c) - D(r, c)]^2}{\sigma^2} \quad (7)$$

where $M(r, c)$ is the model for the cluster spatial and color distribution and Λ_N is a measure of the cluster richness. In this work, we take $M(r, c) = \Sigma(r/r_s)G_{g-r}G_{r-i}$, described in equations (3) and (5). This is essentially the contribution of a galaxy with colors c , at a physical radius r to the likelihood that a test point is in a cluster ridgeline. The uncertainty, σ^2 , is Poisson since the number counts in the aperture are dominated by background, $b(c)$. The Poisson nature then implies $\sigma^2 \simeq b(c)$. We note that the Gaussian approximation is assumed in Eq. 7; since the counts are essentially Poisson distributed with a high mean, the Gaussian approximation is sufficient.

We have on hand a survey containing galaxies with colors and magnitudes, c and m , and radial distances r from a point of interest. Sitting at some point in the survey, the likelihood is evaluated over the full survey, $D(r, c)$, such that:

$$\ln \mathcal{L}_R \propto \int_{Area, c} \left(\ln \sigma + \frac{[b(c) - D(r, c)]^2}{\sigma^2} + \frac{[\Sigma(r/r_s)G_{g-r}G_{r-i}]^2}{\sigma^2} \right) \quad (8)$$

It is apparent in the previous sections that the relevant quantities in the likelihood are all functions of redshift. The models for the colors and the angular scale of the spatial filter will be set after a redshift is chosen for likelihood evaluation (§3). Given that $\sigma^2 \simeq b(c)$, Postman et al. (1996) have shown that maximizing this quantity is nearly the same as maximizing

$$\ln \mathcal{L}_R \propto \int \frac{\Sigma(r/r_s)G_{g-r}G_{r-i}}{b(c)} d^2r dm dc \quad (9)$$

The integral is evaluated by taking the input galaxies to be δ -functions at the radii and magnitudes at which they are observed. This turns the integral into a sum over all the galaxies in the survey (Eq. 10). This likelihood equation is then applied in following manner: Sit on some galaxy in the survey, a “potential” BCG (section 2.4) at a location θ . Look at each neighboring galaxy, k , of N_g total neighboring galaxies. Each neighboring galaxy has colors c_k , and projected distance r_k from the potential BCG. Compute the product $\Sigma(r/r_s)G_{g-r}G_{r-i}$ for each neighboring galaxy, and sum:

$$S(\theta) = \sum_{k=1}^{N_g} \Sigma[r_k(\theta)]G_{g-r}(c_k)G_{r-i}(c_k) \quad (10)$$

The sum $S(\theta)$ consequently embodies the measure of a galaxy’s environment, and serves as the ridgeline likelihood.

2.4. BCG Likelihood

2.4.1. Brightest Cluster Galaxies

The second component of the full maxBCG likelihood is \mathcal{L}_{BCG} , the likelihood that a galaxy is a brightest cluster galaxy. By definition, every cluster has a BCG, and it usually takes the form of a luminous early-type galaxy with an $r^{-1/4}$ surface brightness profile. In some cases the BCG is a giant “cD” galaxy, whose surface brightness is shallower than $r^{-1/4}$ at large radii, forming the cD-envelope. Their luminosities can reach $\sim 10L_*$ and the

envelopes can extend up to 1 Mpc (Hoessel & Schneider 1985). Particularly in the richest clusters, these galaxies comprise a statistically-distinct population (Hansen et al. 2005; Loh & Strauss 2006). In measuring the cluster luminosity function, Hansen et al. (2005) have shown that excluding the BCG markedly improves the fit to a Schechter function, and that the BCG luminosity function is approximately Gaussian. The contrast between BCGs member galaxies for poorer systems is less evident.

Because of the rarity of clusters, galaxies with BCG properties are themselves rare. Using this extra information increases the fidelity of cluster finding. With this likelihood, we look for individual galaxies with specific properties, and fold this in with a measurement of their environment as specified by the ridgeline likelihood. As in Loh & Strauss (2006), who statistically selected BCGs from the SDSS LRG sample on the basis of local density and magnitude, we find that average BCGs make up the bright tip of the red-sequence. Their location in the E/S0 ridgeline is clear in ridgeline plots in Figure 1.

In an effort to study the ubiquity of BCGs, and quantify the characteristics of BCGs, the combined NORAS-REFLEX sample described in Koester et al. (2006) was used to conduct a preliminary visual inspection of the 99 clusters from this combined catalog. We find that 79/99 ($\simeq 80\%$) of the clusters in this sample exhibit a single distinct BCG. Of the remaining 20 clusters, 15 display 2 BCG-like galaxies, and the remaining 5 have no clear BCG and are in fact rather optically-poor. A handful of those with 2 BCG-like galaxies appear as if they are two separate systems undergoing mergers. Of the 79 distinct BCGs, 74 are within ± 0.1 in $g - r$ of the ridgeline for the cluster ($\simeq 94\%$), and 82 out of the full sample of 99 fell within the ridgeline ($\simeq 83\%$).

The BCGs in these clusters fall very near the X-ray centers as well. The median separation of the 79 distinct, visually-identified BCGs, is $54h^{-1}$ kpc. When we add in the clusters with 2 BCGs, the median separation rises to $77h^{-1}$ kpc, and the median separation of the full 99 clusters is $220h^{-1}$ kpc.

The reader is also referred to Koester et al. (2006), where it is revealed that in the final cluster catalog, the maxBCG algorithm centers clusters within a median $57h^{-1}$ kpc of the X-ray center for this same NORAS-REFLEX sample.

Taken together, these results demonstrate that classical BCGs fall within the E/S0 ridgeline better than 90% of the time, and that they are quite near the center of the cluster, both of which are encouraging for the task at hand. Nevertheless, the complex nature of the cluster environment creates exceptions to this pattern, and this must be kept in mind as \mathcal{L}_{BCG} is folded in the maxBCG technique.

2.4.2. BCG Model

\mathcal{L}_{BCG} is calculated independently of environment. Our goal is to tune maxBCG to find rich clusters, and to center those clusters on the cD-like BCGs. Thus, we need to build a sizable sample of training BCGs, enough to generate a model for the colors and magnitudes of such objects. This observationally-driven model is constructed in two steps. First, fiducial BCGs are chosen by constructing a template consisting of bright ($M_r < -21$) LRGs and their distribution in $g-r$, $r-i$, i , and z space modeled with a linear combination of Gaussians fit by expectation maximization algorithm (Connolly et al. 2000). Below $z = 0.15$, the SDSS spectroscopic sample was used to select LRGs similar to ridgeline calibration in §2.3. The maxBCG cluster finder is then run with these bright LRGs serving as the BCG model for \mathcal{L}_{BCG} . Then, to construct a refined BCG model, a set of visually identified BCGs from the richest clusters across $0.1 < z < 0.3$ are chosen from this first run. We identify 100 BCGs in rich clusters with a characteristic cD envelope, and a single nucleus. Because of their luminosities, most have spectroscopic redshifts in the SDSS, so that it is possible to track their colors and magnitudes as function of redshift.

The r -band magnitudes are plotted as a function of redshift for these BCGs in Figure 3. In this figure, note that we plot the r -band for comparison to the study of Loh & Strauss (2006), but in practice we use the i -band magnitude (see §2.5 and the Discussion). There is a clear trend of magnitude with spectroscopic redshift. We fit a quadratic function to this relation, and use it as our model for the trend of BCG magnitude with redshift. The slope of this magnitude–redshift relation is nearly identical to that in Loh & Strauss (2006), with an offset to brighter magnitudes, as expected. The BCGs from rich objects in the full maxBCG catalog in (Koester et al. 2006) (greyscale, Figure 3) display a magnitude–redshift relation similar in shape to that found by Loh & Strauss (2006).

The BCG colors evolve with redshift in essentially the same way as the ridgeline does (see Figure 1 for examples of BCGs in the color–magnitude relation). This is consistent with the results Weinmann et al. (2006), who show that on average, central galaxies properties correlate well with their satellite properties.

The likelihood, \mathcal{L}_{BCG} , is specified to be

$$\mathcal{L}_R(z) = G_{g-r}^{BCG}(z)G_{r-i}^{BCG}(z)e^{-((m-m_i)/\sigma_c)^2}. \quad (11)$$

As mentioned above, the Gaussians G_{j-k}^{BCG} are nearly identical to their ridgeline-likelihood counterparts. A crucial component of this likelihood is the smooth cutoff function that ensures that a galaxy’s luminosity (indicated by its i -band magnitude) is high enough to be a BCG at a given redshift. The cutoff, m_i , is taken from the i -band magnitude–redshift relation, similar to that for the r -band in Figure 3. The width σ_c , is taken from Loh & Strauss

(2006) to be 0.3 magnitudes. Fitting in this way to rich clusters makes us most sensitive to the richest clusters that harbor these BCGs, and further boosts their cluster likelihoods relative to poorer systems. Through visual inspection, we find that this component of the maxBCG likelihood is most effective in properly centering clusters on what one would manually classify as the BCG.

2.5. Input Galaxy Catalog

For ease of processing, the input catalog is broken up into redshift-dependent slices. In each slice we include galaxies whose colors are within 3σ of the predicted $g - r$ and $r - i$ colors. A redshift-dependent lower magnitude limit is also imposed in each slice, such that galaxies with luminosities down to some L_{min} are measured for each cluster, regardless of redshift. This requirement reflects the wish to measure richnesses and find clusters in a manner that does not depend on survey flux limits.

We define the cutoff magnitude, $a(z) + M_*$, which is designed to consistently select objects above M_{min} at all redshifts we consider. M_* is drawn from the galaxy luminosity function in clusters, and $a(z)$ embodies distance, k -correction, and evolution of M_* . This cutoff is selected so that at the redshift limit of the catalog, objects of brightness $a(z) + M_*$ have small photometric errors and are still well within the ridgeline of typical clusters. We work in the i -band when applying these cuts, as the 4000\AA break at $z < 0.3$ stays well out of the range of the i -band, which is centered at $\simeq 7400\text{\AA}$. The typical early-type spectra red-ward of 5000\AA are relatively flat compared to the break, so this minimizes differences in luminosity estimates that would be due to large spectral features moving into and out of bands.

We will shortly determine $a(z)$, but first it is instructive to consider the relevant magnitude range we wish to target. M_*^r in the r -band for the galaxy population is -20.44 (Blanton et al. 2003), at $z \simeq 0.1$, and rises to -20.75 in rich clusters (Hansen et al. 2005). Using Table 1 in Eisenstein et al. (2001) for the non-star-forming galaxy model, we can convert this characteristic r -band magnitude for rich clusters to an approximate i -band magnitude, M_*^i , at $z = 0.1$. For this combination, $M_*^i = -21.24$, which implies a luminosity $L_* = 2.3 \times 10^{10} h^{-1} L_\odot$. For the galaxy catalog we use in Koester et al. (2006), a cutoff of $0.4L_*$ is chosen, for which the maximum magnitude of the input galaxy catalogs we have on hand, corresponds to a redshift limit of ~ 0.40 . For the rest of this paper, we refer to this $0.4L_*$ as “ L_{min} ”.

To actually determine the appropriate k -corrected magnitude cut at each redshift range

of interest, we use a Pegase-2 stellar population/galaxy formation model, similar to that of Eisenstein et al. (2001). Briefly, a range of plausible scenarios was run until the color distribution was very near that of the LRG/BCG colors. A very metal-rich non-primordial gas model was chosen, and predictions for the i -band magnitude of an L_{min} galaxy over the range of redshifts was output. The characteristic magnitudes and luminosities are set at $M_*^i = -21.22$ in this model, which corresponds to $2.25 \times 10^{10} L_\odot$. This compares well with the value of $M_*^i = -21.24$ derived from the observed cluster luminosity function. The corresponding L_{min} , as defined above, is then $0.9 \times 10^{10} h^{-1} L_\odot$, with an absolute magnitude of -20.25 in the i -band. These outputs are saved as our redshift-dependent magnitude limit $a(z) + M_*$.

One final magnitude-dependent step is enforced when actually running the algorithm. In evaluating \mathcal{L}_R to test some galaxy for its similarity to a BCG, only galaxies with apparent magnitudes dimmer than that of the potential BCG are included in \mathcal{L}_R . This works in concert with \mathcal{L}_{BCG} to select clear BCGs more reliably; if there are two bright galaxies with otherwise nearly equal likelihoods, the dimmer one will almost always receive the lower ridgeline likelihood, by virtue of the fact that \mathcal{L}_R increases with the number of galaxies evaluated. It also reduces the number of bright foreground galaxies evaluated in the likelihood function or included in the cluster membership. This cut only depends on the magnitude of the object being tested as a BCG, and not the redshift.

3. Evaluating Likelihoods

As an alternative to pixelization of the galaxy catalog, every galaxy in the survey is tested as a potential cluster center, and the likelihoods are computed considering the possibility that any other galaxy could be a member galaxy of the potential cluster. To speed up computation, the following exceptions are made (in the following, galaxies being evaluated as BCGs at clusters centers are called “candidate BCGs” and objects evaluated in the cluster likelihood are called “neighbors”):

1. To be considered as a center, the candidate BCG must lie within $\pm 3\sigma$ in $g - r$ and $r - i$ of the predicted ridgeline colors at the assumed redshift, and brighter than L_{min} .
2. A neighbor galaxy must be within projected $3 h^{-1}$ Mpc of the center.
3. A neighbor galaxy must be within $\pm 3\sigma$ in $g - r$ and $r - i$ at the test redshift, brighter than L_{min} , and dimmer than the candidate BCG.

In all these cuts, σ is given by Eq. 6 for the appropriate color. The goal is to eliminate

objects whose colors, magnitudes, and angular separations are clearly inconsistent with being red-sequence galaxies at the test redshift. A consequence of item (1) is that each candidate BCG is tested at a range in redshift of $\sim z \pm 0.05$, which we find is adequate to map out the maximum in the likelihood. Figure 4 shows the shape of these likelihood functions vs. redshift for a previously unknown maxBCG cluster at $z = 0.23$. In Figure 5, the SDSS image (see online Journal for color version) is shown, centered on a bright BCG with a preponderance of red galaxies nearby.

Each object in the survey is considered for its likelihood to be a BCG in this way, using the likelihood functions to determine its likeness to a BCG and its environment at a range of redshifts. A maximum-likelihood redshift is assigned by

$$\mathcal{L}_{tot}(z_{max}) = \max(\mathcal{L}_{tot}(z)) \quad (12)$$

(see Figure 4, vertical dotted line), and the overall likelihood that an object is a cluster center is

$$\mathcal{L}_{tot}^{max}(z) = \mathcal{L}_R(z_{max})\mathcal{L}_{BCG}(z_{max}). \quad (13)$$

The result is a list of candidate BCGs with maximum-likelihood redshifts, z_{max} , and maximum cluster likelihoods \mathcal{L}_{tot}^{max} . Each object on the list is marked as a candidate cluster center, with a richness N_{gals} and a scaled richness N_{gals}^{r200} (see the beginning of §2). Its “members” list includes galaxies within a projected separation of r_{200} , 2σ of the ridgeline colors, brighter than L_{min} , and dimmer than the candidate BCG.

By these means, all galaxies within the specified color–magnitude range in the survey are tested as candidate centers. In a typical rich cluster, dozens of members will have been evaluated as potential centers. To build the final cluster list from these candidate centers, the candidate centers are first sorted by decreasing total maximum likelihood. The top object on the list is taken as the BCG of a cluster. All other objects with 1) maximum likelihoods less than this object, 2) redshifts within ± 0.02 (the approximate redshift precision for all richnesses) and 3) within r_{200} of the object, are flagged and prevented from seeding new clusters. The next object on the list is treated in a similar way, and by this simple percolation process, candidate BCGs are flagged whenever they fall within the confines of a higher likelihood object. This process descends all the way through the list of candidate BCGs. The remaining unflagged objects enter the final cluster catalog. In the studies presented herein, we truncate the process at objects with $N_{gals}^{r200} = 10$ and less. While weak lensing and dynamical mass estimates (McKay et al. 2006; Sheldon et al. 2006) indicate the lower richness objects really do trace lower-mass systems, it is not clear what other selection effects may be taking place below this limit. In particular, below the average mass for this limit, some groups may have less well-defined red-sequences and central galaxies that have

different properties. An important feature of the execution is that the reported center of the cluster lands on a cluster galaxy, which typically has the characteristic properties of a BCG.

Figure 6 shows the local value of the composite likelihood function in a 1-degree field centered on Abell 1689. A double peak, corresponding to two galaxies near Abell 1689’s center, is located at (ra,dec) of (197.87, -1.34). The SDSS image of Abell 1689 is shown in Figure 7. Two other previously-identified clusters, one X-ray, one optical, fall in this same field and are easily singled out. Their images are shown in Figures 8 and 9. The large number of peaks with $10 < \mathcal{L}_{tot}^{max} < 100$ correspond to group-sized objects, many of which are absorbed as members of the higher likelihood cluster-sized objects.

4. maxBCG Selection Function

A cluster catalog is only useful for cosmological constraints insofar as its purity and completeness can be understood, both as a function of redshift and of halo mass and/or halo richness. Such measurements have typically been made in X-ray and optical cluster-finding algorithms by Monte–Carlo methods, in which galaxies (or X-ray photons) with various radial distributions are inserted into a suitable background (Postman et al. 1996; Gal et al. 2003). The specific parameters of the model are usually varied to demonstrate an insensitivity of the measurements to the particular choice of parameters.

Here, we begin by taking the Monte–Carlo approach, following a technique similar to that described in Goto et al. (2002). To quantify completeness, we first shuffle input SDSS galaxy catalogs (see Koester et al. 2006) by randomly reassigning galaxy colors and smearing the positions by $5'$. We insert artificial clusters in the following way: 1) at five discrete redshifts, $z = 0.1, 0.14, 0.18, 0.22$, and 0.26 , we extract photometric data for Abell clusters in the SDSS. 2) After background subtraction, we measure the average color and radial distributions of the Abell clusters stacked at these five redshifts (Koester et al. (2007)). 3) At each redshift, the radial distributions, are fit with power laws, and the color distributions are fit with 4th-degree polynomials. 4) To ensure a realistic richness and redshift distribution in the artificial cluster catalog, clusters are constructed by randomly choosing a redshift and richness from the actual maxBCG cluster distribution (Koester et al. 2006). The most nearby of the 5 discrete redshifts is chosen as a suitable model for the color and radial distributions of clusters at that redshift; k-corrections are applied to the colors so that they are actually consistent with the randomly chosen redshift (v4.1.4 of KCORRECT, Blanton et al. (2003b).) 5) A total of 15,000 clusters are inserted into the shuffled background, and maxBCG is run on the resulting galaxy catalogs. To determine if an artificial cluster is found by these means, we ask for each artificial cluster, “is there a maxBCG cluster within ± 0.025 in redshift and

$N_{gals}^{r200} \geq 10$? If so, the cluster is considered detected.

In Figure 10, 90% completeness is reached in all redshift ranges by $N_{gals}^{r200} = 20$. The decreased completeness below this range is partially due to the fact that the artificial clusters were constructed to statistically represent rich Abell clusters, and not the poorer group-sized systems we also wish to detect with maxBCG.

To measure the false-positive rate, we simply run maxBCG on the same shuffled galaxy catalogs constructed above. At $N_{gals}^{r200} = 10$, we detect 178 clusters, compared to the 2558 in the maxBCG catalog described in Koester et al. (2006), for a 7% false-positive rate. At $N_{gals}^{r200} = 15$, the rate is 1%, and is $< 1\%$ by $N_{gals}^{r200} = 20$. Two clusters at $N_{gals}^{r200} = 21$ are the largest systems detected in the shuffled catalogs. The false-positive rate is indeed small.

Using traditional methods to evaluate completeness and purity, the maxBCG algorithm fares very well. However, to more fully assess the catalog’s quality, we employ mock galaxy catalogs largely designed for the purpose of understanding maxBCG selection effects, whose galaxy distribution based on the underlying dark matter distribution and tuned to match observed luminosity-dependent and color-dependent galaxy clustering measurements (Wechsler et al. 2006a). There are two motivations for proceeding in this way. First, compared to simple Monte-Carlo realizations, the mock catalogs are more representative of galaxy clusters in the universe, and will reveal a more realistic picture of the performance of the cluster finder. While any given mock catalog is unlikely to be a perfect representation of the Universe, as we do not understand everything about the physics of galaxy formation and galaxy bias, the closer such catalogs can be, the more robust our understanding of the cluster-finder selection effects can be. These mocks have a strong advantage over previous simplistic methods in that they embed their clusters in a realistic network of filaments and voids, a feature essential for understanding the effects of projection on cluster finding. Secondly is that much of our understanding of large-scale structure is embodied in N-body simulations, and the strength of cosmological constraints comes from understanding the connection of observables with dark matter halos in these simulations. Thus mocks that correctly encode this connection are essential to extract the full power of these data. Ideally, our simulations would directly predict galaxy properties and their distribution from first principles, but we are currently a long way from a complete theory of galaxy formation that can do this robustly. Empirical simulations that connect very realistic galaxy distributions with dark matter halos are the first step towards this eventuality, and allow us to compare observations directly to such simulations.

We establish for the remainder of this work the following definitions: a *halo* refers to an object in the mock catalog, consisting of dark matter and constituent galaxies. A *cluster* refers to any object output by the maxBCG algorithm, whether it is run on real data or on

the mock catalog. As part of this exercise, we use richness definitions particular to halos and derived clusters separately. In Table 1, we provide a summary of the various quantities we employ. The halo-specific measurements include the mass (M_{200}), an intrinsic “true” richness of the halo, as assigned in the mock catalog (N_{int}), and the richness of red galaxies in these halos, N_{int}^{red} . This latter quantity is aimed at describing the richness of each halo as it would be seen by maxBCG in an ideal case: given the halo’s redshift, the number of galaxies from N_{int} is computed by creating a color–magnitude box centered on the E/S0 ridgeline colors, 2σ wide. The cluster-specific measurements, N_{gals} and N_{gals}^{r200} , have already been defined.

MaxBCG is run on the mock catalog in an identical way to how it is run on the real data. We present a naive comparison in Figure 11. The halo abundance in bins of N_{int}^{red} is compared to the N_{gals}^{r200} distribution of the derived maxBCG clusters from that simulation. For reference, $N_{int}^{red} = 100$ objects have masses of $M_{200} \sim 1 \times 10^{15}$, and $N_{int}^{red} = 50$ objects have masses of $M_{200} \sim 5 \times 10^{14}$. In principle, N_{int}^{red} of halos is similar to N_{gals}^{r200} , in that they use the same color cuts, and have a physical scale associated with them.

The abundances are approximately consistent in their slopes, but there appears to be an overabundance of clusters at all richnesses. This could be due to the performance of the cluster finder itself, wherein it tends to merge smaller systems along the same line of sight. It could also possibly stem from small-scale projection effects that would cause maxBCG to overestimate the halo richness, making N_{gals}^{r200} an overestimate of N_{int}^{red} . In the next section, these possibilities as well as others are investigated.

4.1. Completeness and Purity

As part of the output of maxBCG, we include cluster members, which are galaxies within a certain spatial distance of the BCG and inside a color–magnitude box appropriate to the maximum likelihood redshift. As these are predominantly red-sequence galaxies, a large fraction are physically associated with the cluster, at around the 80% level, as indicated by spectroscopy (Koester et al. 2006). The members are thus good indicators of the cluster’s position in physical space, so we use them as such when comparing to the simulations. The same goes for the mock galaxy catalog: halo galaxy members are good indicators of the halo positions, as they all sit with r_{200} of the halo. We thus wish to use the overlap between halo galaxies and cluster galaxies to assert whether or not a halo in the simulation is “matched” to a cluster returned by maxBCG. In the same spirit as N_{int}^{red} , we only consider red halo members, i.e. the exact galaxies that make up N_{gals}^{red} are considered halo members.

In this exercise, we consider runs of maxBCG on three mock galaxy catalog realizations of the same cosmology in the interests of minimizing sensitivity to statistics. We restrict ourselves to a cluster catalog with objects of $N_{gals}^{r200} \geq 10$, and $0.08 < z < 0.32$, as this is the final cut applied to the catalog presented in Koester et al. (2006). The halo catalog includes halos of $M_{200} > 5 \times 10^{13}$ solar masses and redshifts $0.1 < z < 0.3$. To aid in the interpretation, we first note that this mass limit corresponds to an average $N_{int}^{red} \simeq 5$ and $N_{int} \simeq 10$. The redshift correspondence between “matched” (see below) clusters and halos is quite good, but the fact that there is some scatter between the maxBCG photometric redshift and the halo redshift (Figure 12) should be accounted for in the interpretation.

To measure the completeness, we ask the question “for a given halo, which cluster contains the largest fraction of the red halo galaxies?”. Call this fraction f_h , and the cluster that satisfies this criteria, the “best” match. We can define a threshold for f_h below which we consider a halo to remain unmatched. For this exercise, we choose f_h as follows: First, note that the cluster membership criteria counts bright red galaxies within r_{200} , and in the simulations, halo richness is also computed inside an r_{200} value determined from the *darkmatter* profile. When matching, only the bright red halo galaxies inside r_{200} are considered. The median r_{200} of the dark matter halos with $M_{200} > 8 \times 10^{13}$ is $r_{200} = 0.95$ Mpc. However, that used in maxBCG for clusters with 10 or more red galaxies is 0.88 Mpc, so that ratio of the areas is $0.88^2/0.95^2$, or $\simeq 0.3$. Thus, $f_h = 0.3$ is an appropriate threshold.

In Figure 13, we choose a threshold of $f_h = 0.3$, and display contours of completeness across the full redshift and mass range of halos. Evidently, maxBCG exhibits a very high completeness at high mass, which begins to decline at around $2 \times 10^{14} h^{-1} M_\odot$. Many of these “missed” objects are assigned $N_{gals}^{r200} < 10$, which excludes them from the richness cut we make here, a manifestation of the mass-richness scatter. Indeed, at $8 \times 10^{13} h^{-1} M_\odot$, there are only about 5 red galaxies in a typical mock halo.

It is safe to conclude that maxBCG locates clusters with high completeness down to at least $M_{200} = 2 \times 10^{14} M_\odot$, and certainly identifies a large population of even lower mass objects. Thus, our stated completeness is quite conservative; in particular if completeness were defined without this explicit cut in richness it wouldn’t decline at these masses (see Rozo et al. 2006 for a discussion).

Figure 13 also reveals that the cluster catalog includes halos with $z > 0.3$, nearly at the edge of the simulation. Although these halos are within the redshift error of maxBCG ($\sigma_z \simeq 0.015$, Koester et al. (2006)), they introduce a level of contamination to the final cluster catalog. The same could be said for lower mass halos being misidentified as higher mass halos, but the interpretation is less clear, as the mass-observable scatter is quite large; the identification of low mass halos could still be within the limits of the mass-observable scatter

without actually being contamination.

The purity is defined here by asking the reverse question: “for a given cluster, which halo contains the largest fraction of the cluster members?”. This fraction is f_c , and the halo that satisfies this criteria is the “best” halo match. A threshold at $f_c = 0.3$ is chosen for defining a match, and the purity contours in richness and redshift space are shown in Figure 13. At redshift edges of the catalog, the purity declines slightly. This is due to the fact the halo catalog we match to is truncated at $z = 0.3$ and $z = 0.1$, the range we are concerned with at present. Thus there are some clusters with photometric redshifts that place them within the redshift bounds of the cluster catalog, but whose associated halos have true redshifts just outside this range. This is evident in the scatter of the halo-to-cluster redshift correspondence shown in Figure 12. We can confidently say that over the range of the catalog, the purity is well over 90%.

4.2. Richness Scaling

In the case of completeness, it is not enough to simply say that all halos above some mass threshold were “found”. By the matching executed above, a massive halo with a high N_{int}^{red} could be matched to a cluster with low N_{gals}^{200} . While this is considered “found”, ideally a halo that was successfully flagged by the cluster finder would be associated with a cluster of a richness that is reflective of the halo’s richness. In this sense, we can take the matching exercise a step further and ask “how well does the richness of the best matched cluster reflect that of the underlying halo?”

In the top panel of Figure 14, halo richnesses and the richness of the best-matched cluster are compared for one of the mock galaxy catalogs. Each halo is represented by a cross or a diamond. Halos represented by crosses are those that were the most massive match to each cluster. Halos represented by diamonds are those that were matched with clusters that had already been previously matched by a larger halo. Following Gerke et al. (2005), we call this “overmerging”. There is a large population of halos with well-matched clusters, i.e., clusters with richnesses indicative of the underlying halo properties. However, there is a subset of overmerged halos (diamonds) with low N_{int}^{red} and high N_{gals}^{200} . Naively, this may be attributed to catastrophic projection effects that have been known to plague optical cluster finding. This in turn could mean that we have clusters we think are rich, but really are just projections of many random things along a deep line of sight. But there is another possibility. Our likelihoods will not resolve halos within a few Mpc of each other, along the line of sight, particularly large halos with a few smaller neighbors. Thus maxBCG can merge these objects, selecting one large, dominant halo and merging the smaller neighbors.

Members from these neighboring halos overlap strongly with the cluster members from the dominant cluster, so all the halos match to the *same* cluster. This explains the low N_{int}^{red} , high N_{gals}^{200} population seen in Figure 14.

The three boxed points at the of the top panel of Figure 14 illustrate this merging. They are three separate halos of masses 1.03×10^{15} , 6.57×10^{14} , $3.94 \times 10^{14} M_{\odot}$, N_{int}^{red} of 89, 62, and 38, redshifts at 0.233, 0.229, and 0.235. The latter two appear as diamonds. These halos are in fact all within $< 7.1 h^{-1}$ Mpc of each other, approximately along the same line-of-sight. This physical distance is below the resolution we expect to gain from the red sequence. The cluster that is best matched to all three of these halos has $N_{gals}^{200} = 269$, greater than the sum (189) of these three halos. A large portion of the objects in this region of Figure 14 are less severe instances of this same type of overmerging. But the matching algorithm used here generally associates rich clusters with rich halos, so our quoted completeness is dually informative. These smaller halos (diamonds) are evidence that maxBCG is performing as expected, merging smaller, nearby halos with larger ones.

To further elucidate the situation, the question can be turned around: “how well does the richness of the best matched halo reflect that of the underlying cluster?”. This asks the same question of cluster-to-halo matching for the purity measurements. In the lower panel of Figure 14, for each cluster, we plot cluster N_{gals}^{200} and the N_{int}^{red} of the best matched halo. This selects one best halo for each cluster. The excess at low N_{int}^{red} and high N_{gals}^{200} seen in the top panel vanishes, which shows that indeed those small halos (diamonds in the upper panel) were not poorly matched, but that they were absorbed into large clusters. The case described above of extreme overmerging shows up as one point at (89,269).

The diamonds that appear on the lower panel are clusters that were matched to a halo which had already been claimed as best match by a richer cluster. This *fragmentation*, in which the halo is broken up by maxBCG, is much less prevalent than overmerging (this is quantified in the following section). When fragmentation does occur, there is still generally one large halo matched to one large cluster, with a few smaller clusters in the neighborhood as well.

The most interesting case to study here is the two clusters with $N_{gals}^{200} = 223, 15$, and redshifts 0.170, 0.173. These two correspond to one halo, with a mass $M_{200} = 1.726 \times 10^{15} M_{\odot}$, $N_{gals}^{red} = 163$, and $z = 0.167$. There is one clear dominant cluster here, and two others with much smaller richnesses. This is a case of fragmentation, but it is not especially problematic because there is still a dominant cluster associated with the halo. This same dominant cluster shows up in the top panel of Figure 14 at (163,223).

It is safe to conclude then that we are successfully matching rich clusters and rich halos,

and that our completeness and purity measurements are telling us much more than “did we find all the halos” and “is there a halo there or not?” By either means, rich halos are associated with rich clusters. We note that this is encouraging for mass calibration. The extension of these results to understanding the mass-richness relation is enticing, and is undertaken using observational weak lensing and dynamical measurements in other works (McKay et al. 2006; Sheldon et al. 2006; Koester et al. 2006).

We conclude this section by applying the insight gained from looking at the richnesses to the abundances seen in Figure 11. In Figure 14, we display best-fit lines to richness relations. If the offset in the abundances is really due to a disagreement between the maxBCG N_{gals}^{r200} richness and the intrinsic N_{int}^{red} , and the line is a good fit, then the line should supply the transformation between the two, using either fit. In the upper panel, the best-fit line has a slope 1.409 ± 0.013 and intercept 1.227 ± 0.190 . This tells us how we should transform N_{int}^{red} for the halo abundance to N_{gals}^{r200} . If it is perfect, it should shift the halo abundance curve onto the maxBCG abundance. In the lower panel, the best-fit line has slope 0.601 ± 0.005 and the intercept 1.028 ± 0.160 , telling us how to transform the N_{gals}^{r200} in the maxBCG abundance to N_{int}^{red} . If this transformation is perfect, it should shift the maxBCG abundance into agreement with the halo abundance. Overplotted on Figure 11 are resulting abundances under the transformation of N_{int}^{red} to N_{gals}^{r200} (upper dotted line and upper panel of Figure 14) and the reverse transformation (lower dotted line and lower panel of Figure 14). The latter transformation nearly brings the maxBCG abundance into agreement with the intrinsic halo abundance, while the former transformation brings the halo abundance into agreement with maxBCG only at low richness. From Figure 14, the duplication present in the upper panel alerts us to the difficulty in seeking a simple relation between the richnesses, but the relation is more straightforward from the reverse situation in the bottom panel. Without further modeling of this relationship, we can assert now with confidence that the offset in the abundances observed in Figure 11 is largely due to differences in the richness measurement.

4.3. Fragmentation and Overmerging

Measurements of the cluster abundance function or of cluster clustering are potentially powerful cosmological tools. A standard assumption is to assume that each cluster from the cluster catalog can be matched uniquely to one halo. The extent to which this is true depends on the cluster finder, and the definition of the halo (Kim et al. 2002; Gerke et al. 2005). For instance if the cluster finder assigns two clusters to each halo, an inflated abundance function will result, as well as a correlation function with increased amplitude. A full treatment of

this relationship depends on the exact scientific goal one wishes to address. We explore this question in detail, as it applies to cosmological constraints from the cluster abundance function in Rozo et al. (2006). In this section, some relevant issues for such modeling are described.

Up to this point, we have taken the “best” match of halos to clusters and vice-versa to measure the purity and completeness respectively. Using these methods, it is possible for a halo to have, say, 70% of its members come from one cluster, 20% from another, and the remaining 10% not associated with any cluster. In cases where the fractions become nearly equal, say, 50/45/5, there is no clear one-to-one association. This was touched upon in 14, where our matching prescription revealed examples of halos being merged into several clusters, and a few of the opposite, where halos were broken up into two or three clusters.

To evaluate the fragmentation incidence, we take a halo and look at the top two clusters that contributed members, the “best” and the second best. We create a simple fragmentation diagnostic:

$$\phi_h = \frac{N_2^h}{N_1^h} \quad (14)$$

where N_1^h and N_2^h are the numbers of members contributed by the best and second best cluster matches. $\phi_h = 0$ when $N_2^h = 0$ and there is no fragmentation, and $\phi_h = 1$ when the halo was perfectly broken in two. This distribution is shown as a function of N_{int}^{red} in the top panel of Figure 15. To understand the distribution better, we bin the halos by richness and report the median of ϕ_h in each richness bin (solid line) It quickly approaches 0, indicating that there is a minimal amount of fragmentation. The fragmented halo at $N_{gals}^{red} = 163$ shows up as a point at (163,0.2) in this panel. Out of 112 halos with $N_{gals}^{red} > 50$, 7 have $\phi_h > 0.1$, or 6%. For $N_{int}^{red} > 10$, this rises to 25%.

The exercise is repeated for clusters, considering the top two halo matches. The over-merging statistic, ϕ_c is shown in Figure 15, lower panel. The median hovers around 0.2, indicating that there is some over-merging present in the catalog at all richnesses. It is clear that there is a population of clusters that consist of overmerged halos. For $N_{gals}^{r200} > 50$, 118/299 halos have $\phi_c > 0.2$, or 39%. The number is slightly lower for the full range of $N_{gals}^{r200} > 10$, at 37%. It thus remains true that imaging based-cluster surveys will be subject to overmerging, as colors have difficulty resolving of order 10 Mpc line-of-sight distances. This is another contribution to the apparent overabundance seen in Figure 11.

More generally, rich clusters with large apertures will be particularly subject to over-merging of systems along the line-of-sight. This is likely true of any imaging survey, and future cosmological analyses using clusters from imaging surveys will require a detailed understanding of the extent to which this influences the final constraints.

4.4. Improved modeling of selection effects

Thus far, we have presented the basic features of the algorithm one must incorporate into any cosmological analysis. The matching routines executed herein are designed simply, so that we can understand the output of maxBCG. However, consideration of the richness estimates and the prevalence of fragmentation and overmerging using the maxBCG algorithm demonstrates that these effects must be modeled in detail to fully understand the selection function and properly model abundances. Rozo et al. (2006) employ a matching algorithm similar in spirit to that presented here, that makes cluster-to-halo associations clearer, and makes the selection function of maxBCG easier to quantify. Figure 15 demonstrates the improvement one can realize in the matching. We refer to this as “exclusive” matching, and point the reader to (Roza et al. 2006) for a full description. Note that exclusive matching does substantially better than the “one-way” matching used in the current work, and in particular that the slope between the cluster abundance and the halo abundance is now roughly unity. We refer the reader to this paper for a detailed discussion of how to calibrate the full connection between clusters and halos in a way appropriate for modeling cluster abundances.

5. Discussion

We have described herein the key components of the maxBCG cluster finder and their origins. The performance of its likelihood functions have been demonstrated in a few case studies of observed galaxy clusters. Over the redshift range of $0.1 < z < 0.3$, its selection function was evaluated as a function of halo mass and cluster richness. The results of the selection function tests were further supported by the demonstration that the maxBCG cluster–mock halo correspondence behaves as expected: rich clusters typically correspond to rich, massive halos. These same comparisons proved to be efficient diagnostics of fragmentation and overmerging. It seems that in addition to the N_{gals}^{r200} richness measurement being an overestimate of richness (Figures 11 and 14), maxBCG tends to overmerge systems along the line of sight (Figures 14 and 15).

5.1. Features of MaxBCG

This algorithm differs from other photometric cluster finders in its use of likelihoods. Earlier methods have used a range of methods to compute cluster likelihoods and assign significances (Postman et al. 1996; Gladders & Yee 2000; Gal et al. 2000). In these methods,

cluster candidates have been selected by assessing the global significance of their likelihoods and then choosing some likelihood threshold above which cluster candidates are selected. These highest significance clusters are then reported in the catalog.

In maxBCG, we set out to push farther down the abundance function by making no such cut. The likelihood function is used locally to report the highest likelihood objects in some region of sky, and then the likelihoods are used to excise locally less significant objects. At no point do we enforce a global likelihood cut, so that the likelihood function is permitted to define objects down to very low richness. Although the completeness and purity are decreased in this regime, the average properties of these lower likelihood, lower richness objects are very encouraging. Their stacked velocity profiles (Koester et al. 2006; McKay et al. 2006) and weak lensing measurements (Sheldon et al. 2006) indicate that they are indeed massive objects whose richnesses are strongly coupled to the underlying mass distribution. This opens up this possibility of leveraging the larger statistics of this lower mass population in constraining cosmology, if the selection effects can be properly understood.

Another fundamental difference in the execution of this algorithm is its reliance on galaxy positions. We evaluate the likelihood function at the locations of galaxies, and not on pixelized data. In pixelization schemes, the data is broken up spatially, and likelihood functions are tested at each pixel. Various means are then used to assess significant peaks in the likelihood function across pixels in the survey, and significant pixels are then tied to clusters. This method helps to speed up the cluster search, and it also prevents over-identification of substructure, or multiple identifications of the same cluster. At the cost of computational time, we find that using galaxy positions allows us to report cluster positions centered on visually-identified BCGs. By our percolation scheme, we do not suffer from over-identification of substructure, which would manifest itself in our fragmentation measurements.

5.2. Background

Recall that we measure cluster properties down to $0.4L_* \equiv L_{min}$ at each redshift. Ideally, the L_{min} cutoffs could be derived empirically from the LRG distribution in the way that the colors were extracted. This requires a full treatment of the luminosity function of LRGs vs. redshift. Obviously, biases in the model could bias the richness measurements and possibly the likelihood functions. The two major sources of bias are incorrect k -corrections and, to a lesser extent, evolution of the luminosity function.

We can take a quick look at the consequences of biases introduced by slight errors in

the offset $a(z)$ of the $a(z) + M_*$ cutoff (see section 2.5). First, at $z = 0$, we can integrate down the cluster luminosity function (Hansen et al. 2005) to $a(z) + M_* = -20.25$ in the cluster’s rest frame. This gives us a count of the number of galaxies, N_c in the cluster brighter than -20.25. Now, imagine we place the same cluster at $z = 0.2$, where the i -band samples a bluer, and possibly dimmer part of the rest frame spectra of the cluster galaxies. K -corrections use a model of the spectra of such galaxies to correct for this systematic offset, but the model may represent this offset with varying degrees of success at different redshifts. Assume that the k -corrections at $z = 0.2$ are too dim by only 0.15 magnitudes on average. Call this error δm . We can again integrate down the same luminosity function, this time to $0.15 + a(z) + M_*$, and get a number of cluster galaxies $N_c + \delta N_c$. Comparing this value to that of the rest-frame (N_c) reveals that the number counts can be 20% higher when the k -corrected limiting magnitude L_{min} is 0.15 too dim. The fractional errors in the number of cluster galaxies for a given magnitude error, δm , can be cast in the following form:

$$\frac{\delta N_c}{N_c} \simeq 1.33 \delta m \quad (15)$$

Thus, when δm varies with redshift, it is clear that the richness estimate and the likelihood function (see next paragraph) can have unwanted redshift dependence built in.

If there are indeed biases in L_{min} , it will certainly affect our richness measurements, but we don’t expect it to bias the cluster finder itself. First, because the \mathcal{L}_R varies slowly with redshift the backgrounds at adjacent redshifts, say $z = 0.2$ and $z = 0.21$, are very similar. Second, the redshift-color relation is smooth and well-understood so that the color filter component of the likelihood function does not radically change. Last, the ridgeline likelihood function is usually strongly peaked as a function of redshift, so that there is an obvious maximum in redshift space. Again, this is not a problem for rich objects, because the detections are robust. Redshift biases are more likely to be seen in low richness objects, where the detections are not high S/N and the background number counts are not well-approximated as Gaussian, and the galaxy population is not as dominated by red-sequence galaxies. Broader spectroscopic samples and realistic mock galaxy catalogs that include more faint galaxies will enable a more systematic study of the effect of background in maxBCG cluster detection.

If there are obvious redshift biases introduced by this method, in particular the model for L_{min} , they will be borne out in the catalog (see Paper I). In particular, for $0.1 < z < 0.3$, the number of objects should increase like the volume enclosed. In the accompanying paper (Koester et al. 2006) we demonstrate that this is approximately the case, and the catalog is volume-limited to $z = 0.3$.

5.3. Model Biases

There are notable exceptions to our model for the BCG colors. A well-known population of so-called cooling-flow clusters contain BCGs where gas is in the process of cooling and forming stars, which creates a significantly bluer BCG. The presence of emission lines in the BCG spectrum provides evidence for a cooling flow. A1835 is a well-known example (e.g. McNamara et al. 2006). While we successfully find such clusters, we do not pick the brightest cluster galaxy as the center because its $g - r \simeq 0.6$ is significantly bluer than the other red-sequence cluster galaxies, which all hover around $g - r \simeq 1.3$. In the BCS X-ray cluster catalog (Ebeling et al. 1998), 27% of BCGs show some sort of emission lines (Crawford et al., 2003). The extent to which emissions lines are prevalent in BCGs living in the cluster population as a whole, and the impact they have on the BCG colors, are questions we can begin to address with maxBCG-selected catalogs. The study of Weinmann et al. (2006), which selects low-redshift groups from spectroscopy without reference to color, hints that BCG colors different from those of the cluster population are the exception rather than the norm.

The matched-filter technique applied here is built around the colors of the E/S0 ridgeline and the NFW distribution expected in clusters of galaxies. The idea is that it should faithfully describe the average properties of galaxy clusters. Certainly, it will discriminate against objects that don’t fit this model, which is more likely to be true at lower mass and richness, and potentially at higher redshift. We can only quantify this in so far as the mock catalogs are a realistic representation of the cluster and background populations. However, it is worth pointing out that any cluster finder that operates on photometric data will have to make some assumptions about the galaxy populations and their distributions, and it is thus worth making these assumptions as easy to understand and as close to reality as possible.

A final note is that the cluster finder requires an assumption about the cosmological dependence of the angular diameter distance and the cluster luminosity function used at various stages of the algorithm. Given a large enough sample with redshifts, the luminosity function could be determined observationally, but for large changes in cosmology, it is less clear what to do about the angular diameter distance. The sensitivity of both of these to cosmology is currently under investigation.

5.4. Photometric Errors

As the redshift of an object increases, so does its photometric error. One would like for the photometric errors to be much less than the intrinsic ridgeline width. As the errors

get bigger, we allow galaxies to be tested as members in more clusters. This can potentially affect the richness by preferentially inflating richnesses at high redshift, where the color errors are larger. The cluster catalog presented in Koester et al. (2006) is approximately volume-limited in all richness bins, which suggests that this effect is not too severe. However, a more well-understood richness measurement comes at the price of the information lost by discarding galaxies with large errors. Appropriately dealing with photometric errors is currently an issue of interest.

5.5. Issues for extending to higher redshift

The SDSS is a goldmine of cluster data, and it provides an important testing ground for algorithms which will generate the cluster catalogs important to cosmological constraints in future surveys. We have restricted ourselves to a redshift range where the clusters are well-measured, and most of the redshift and color information is contained in one band.

The selection is quite uniform across all redshifts, but this may change when the search encompasses $z > 0.35$, as the 4000 Å break migrates in the r -band, and $r - i$ contains more information. Future surveys will aim to find clusters uniformly across a broad range of redshifts, spanning many filters. The likelihoods that embody these color models must weight the different colors fairly, and smoothly handle transitions from one band to another.

The SDSS is deep enough that the same methods provide a means to select clusters out to at least $z \sim 0.6$, and still see the brightest members. Toward this redshift, the flux-limit of the survey becomes an issue in fairly measuring richnesses and evaluating likelihood at all redshifts.

5.6. MaxBCG vs. Other Wavelengths

The results presented here and in Koester et al. (2006) indicate that maxBCG recovers galaxy clusters with purity and completeness levels of 90% for $M > 2 \times 10^{14} M_{\odot}$ and $N_{gals}^{r200} \geq 10$. X-ray selected clusters of similar sky and redshift coverage such as the Brightest Cluster Sample (BCS Ebeling et al. 1998) and the Northern ROSAT All-Sky (NORAS Böhringer et al. 2000) Survey are complete at the 80 – 90% level above a given flux limit which will naturally impose a selection effect on the resulting cluster sample that is strongly dependent on redshift. Redshift-dependent effects in maxBCG arise only through biases in L_{min} over $0.1 < z < 0.3$. Böhringer et al. (2000) reach 76% in purity, as determined through optical follow-up of X-ray selected clusters. The purity of X-ray samples is altered by un-

resolved active-galactic nuclei or stellar contamination, while the purity of optical samples can be compromised by projection.

Aside from the completeness and purity of the sample, understanding the mass distribution of the cluster sample is of utmost importance. From the preceding analysis, it is clear that projection plays a role in both richness estimation and in overmerging. These can both bias the estimate of the mean mass at fixed richness, and the estimate of the scatter. The same can be said of mass estimates in X-ray and SZ surveys: point-source contamination, mergers, and other gasdynamical processes contribute to the overall X-ray signal. No technique is perfect, but for given cluster sample, the extent to which contamination of the observables can be understood will strongly affect the resulting cosmological parameter constraints.

6. Summary

The maxBCG algorithm represents a significant step forward in large galaxy survey cluster detection. Much is known about the properties of cluster galaxies, and the availability of immense, rich, imaging catalogs allows us to begin leveraging this knowledge to detect cleaner and more robust cluster samples and to provide new cosmological information. Since optical surveys in the near future intend to pursue cluster cosmology to varying degrees, the advances presented here are timely. We summarize them as follows:

- MaxBCG pushes beyond the high end of the abundance function, down to group-sized halos, where there is additional cosmological information. The purity and completeness across this broad range are above 90% for $N_{gals}^{r200} > 10$ and $M_{200} > 2 \times 10^{14}$, respectively, across $0.1 < z < 0.3$. Systems below this mass range are quite accessible as well, depending on where one draws the richness cut.
- In addition to spatial clustering of red-sequence galaxies, we add in information about brightest cluster galaxies and multiple colors to refine the search.
- The likelihoods are evaluated at individual galaxies, as opposed to pixelizing the sky.
- The selection function of the algorithm is explored in detail with mock galaxy catalogs. Since the mock catalogs contain a wealth of observationally-motivated information that is coupled to the underlying mass, we are able to undertake an unprecedented study of the performance of the algorithm on individual halos to gain a deeper perspective on the halo selection.

- The mock catalog provides an initial demonstration of the richness–mass mapping; richer systems are preferentially associated with more massive halos.
- We confirm the expectation that on $\sim 10h^{-1}$ Mpc scales, maxBCG tends to over-merge systems projected along the line-of-sight, an effect that will have to be modeled. Fragmentation is not found to be significant.
- We open the discussion of difficulties that will be encountered in future multi-band, wide-angle, high-redshift cluster surveys. Among these are uniformity of the richness measurements, challenges in using multiple colors, photometric errors, and quantification of the selection function.

In an accompanying paper (Koester et al. 2006) and others soon to follow, maxBCG is further assessed with $\simeq 7500$ deg² of SDSS imaging data. In this test on real data, the scaling of cluster richness with velocity dispersion is demonstrated, as are the quality of photometric redshifts, the incidence of projection, the uniformity of richness measurements and the agreement between these optical clusters and earlier X-ray selected catalogs. The maxBCG method provides a different approach to optical cluster selection with a number of useful features. The experience gained in using it on SDSS data will provide important guidance in planning and executing future surveys, such as those planned to study dark energy, including the Dark Energy Survey (The Dark Energy Survey Collaboration 2005), the Panoramic Survey Telescope & Rapid Response System (Kaiser & Pan-STARRS Collaboration 2005), the Supernovae/Acceleration Probe (Aldering et al. 2002), and the Large Synoptic Survey Telescope (Haiman et al. 2004).

Funding for the SDSS and SDSS-II has been provided by the Alfred P. Sloan Foundation, the Participating Institutions, the National Science Foundation, the U.S. Department of Energy, the National Aeronautics and Space Administration, the Japanese Monbukagakusho, the Max Planck Society, and the Higher Education Funding Council for England. The SDSS Web Site is <http://www.sdss.org/>. T. McKay, A. Evrard, and B. Koester gratefully acknowledge support from NSF grant AST 044327. R. Wechsler is supported by NASA through Hubble Fellowship grant HST-HF-01168.01-A awarded by the Space Telescope Science Institute. We are grateful for the repeated hospitality of the Aspen Center for Physics and the Michigan Center for Theoretical Physics.

REFERENCES

Abell, G. O. 1958, ApJS, 3, 211

- Abell, G. O., Corwin, H. G., & Olowin, R. P. 1989, *ApJS*, 70, 1
- Adelman-McCarthy, J. K., et al. 2006, *ApJS*, 162, 38
- Aldering, G., et al. 2002, in *Future Research Direction and Visions for Astronomy*. Edited by Dressler, Alan M. *Proceedings of the SPIE*, Volume 4835, pp. 146-157 (2002)., ed. A. M. Dressler, 146–157
- Allen, S. W., Schmidt, R. W., & Fabian, A. C. 2002, *MNRAS*, 334, L11
- Annis, J. et al. 1999, *Bulletin of the American Astronomical Society*, 31, 1391
- Balogh, M. L., Baldry, I. K., Nichol, R., Miller, C., Bower, R., & Glazebrook, K. 2004, *ApJ*, 615, L101
- Balogh, M. L., Navarro, J. F., & Morris, S. L. 2000, *ApJ*, 540, 113
- Barger, A. J. et al. 1998, *ApJ*, 501, 522
- Barrientos, L. F. 1999, Ph.D. Thesis
- Barrientos, L. F., Schade, D., López-Cruz, O., & Quintana, H. 2004, *ApJS*, 153, 397
- Bartelmann, M. 1996, *A&A*, 313, 697
- Battye, R. A., & Weller, J. 2003, *Phys. Rev. D*, 68, 083506
- Berlind, A. A. et al. 2006, *ApJ*, submitted
- Bernardi, M., Sheth, R. K., Nichol, R. C., Schneider, D. P., & Brinkmann, J. 2005, *AJ*, 129, 61
- Blanton, M. R., et al. 2003, *ApJ*, 592, 819
- Blanton, M. R., et al. 2003, *AJ*, 125, 2348
- Böhringer, H. et al. 2004, *A&A*, 425, 367
- . 2001, *A&A*, 369, 826
- . 2000, *ApJS*, 129, 435
- Bower, R. G., Lucey, J. R., & Ellis, R. S. 1992, *MNRAS*, 254, 601
- Brodwin, M. et al. 2005, *American Astronomical Society Meeting Abstracts*, 206

- Carlstrom, J. E., Holder, G. P., & Reese, E. D. 2002, *ARA&A*, 40, 643
- Connolly, A. J., Genovese, C., Moore, A. W., Nichol, R. C., Schneider, J., & Wasserman, L. 2000, *arXiv:astro-ph/0008187*
- Couch, W. J., Ellis, R. S., MacLaren, I., & Malin, D. F. 1991, *MNRAS*, 249, 606
- Croton, D. J. et al. 2006, *MNRAS*, 365, 11
- Dalton, G. B., Maddox, S. J., Sutherland, W. J., & Efstathiou, G. 1997, *MNRAS*, 289, 263
- David, L. P., Jones, C., & Forman, W. 1995, *ApJ*, 445, 578
- Djorgovski, S. G., Odewahn, S. C., Gal, R. R., Brunner, R., de Carvalho, R. R., Longo, G., & Scaramella, R. 1999, *Bulletin of the American Astronomical Society*, 31, 828
- Ebeling, H., Edge, A. C., Bohringer, H., Allen, S. W., Crawford, C. S., Fabian, A. C., Voges, W., & Huchra, J. P. 1998, *MNRAS*, 301, 881
- Eddington, A. S. 1913, *MNRAS*, 73, 359
- Eisenhardt, P. R. et al. 2005, *American Astronomical Society Meeting Abstracts*, 207
- Eisenstein, D. J., et al. 2001, *AJ*, 122, 2267
- Eke, V. R. et al. 2004, *MNRAS*, 348, 866
- Evrard, A. E. 1997, *MNRAS*, 292, 289
- Gal, R. R. 2006, *arXiv:astro-ph/0601195*
- Gal, R. R., de Carvalho, R. R., Lopes, P. A. A., Djorgovski, S. G., Brunner, R. J., Mahabal, A., & Odewahn, S. C. 2003, *AJ*, 125, 2064
- Gal, R. R., de Carvalho, R. R., Odewahn, S. C., Djorgovski, S. G., & Margoniner, V. E. 2000, *AJ*, 119, 12
- Gerke, B. F. et al. 2005, *ApJ*, 625, 6
- Gioia, I. M., Henry, J. P., Maccacaro, T., Morris, S. L., Stocke, J. T., & Wolter, A. 1990, *ApJ*, 356, L35
- Giuricin, G., Marinoni, C., Ceriani, L., & Pisani, A. 2000, *ApJ*, 543, 178
- Gladders, M. D., & Yee, H. K. C. 2000, *AJ*, 120, 2148

- . 2005, *ApJS*, 157, 1
- Gonzalez, A. H., Zabludoff, A. I., & Zaritsky, D. 2005, *ApJ*, 618, 195
- Gonzalez, A. H., Zaritsky, D., & Wechsler, R. H. 2002, *ApJ*, 571, 129
- Goto, T. et al. 2002, *AJ*, 123, 1807
- Goto, T., Yamauchi, C., Fujita, Y., Okamura, S., Sekiguchi, M., Smail, I., Bernardi, M., & Gomez, P. L. 2003, *MNRAS*, 346, 601
- Haiman, Z., Mohr, J. J., & Holder, G. P. 2001, *ApJ*, 553, 545
- Haiman, Z., Wang, S., Khoury, J., Hennawi, J. F., May, M., Spergel, D. N., & Tyson, J. A. 2004, American Astronomical Society Meeting Abstracts, 205
- Hansen, S. M., McKay, T. A., Wechsler, R. H., Annis, J., Sheldon, E. S., & Kimball, A. 2005, *ApJ*, 633, 122
- Hashimoto, Y., & Oemler, A. J. 1999, *ApJ*, 510, 609
- Hoessel, J. G., & Schneider, D. P. 1985, *AJ*, 90, 1648
- Hogg, D. W. et al. 2004, *ApJ*, 601, L29
- Holder, G. P., Mohr, J. J., Carlstrom, J. E., Evrard, A. E., & Leitch, E. M. 2000, *ApJ*, 544, 629
- Huchra, J. P., & Geller, M. J. 1982, *ApJ*, 257, 423
- Ikebe, Y., Reiprich, T. H., Böhringer, H., Tanaka, Y., & Kitayama, T. 2002, *A&A*, 383, 773
- Kaiser, N., & Pan-STARRS Collaboration. 2005, American Astronomical Society Meeting Abstracts, 206
- Kepner, J., Fan, X., Bahcall, N., Gunn, J., Lupton, R., & Xu, G. 1999, *ApJ*, 517, 78
- Kim, R. S. J. et al. 2002, *AJ*, 123, 20
- Koester, B. P. et al. 2006, *ApJ*, accepted
- Koester, B. P. et al. 2007, in prep.
- Krick, J. E., Bernstein, R. A., & Pimbblet, K. A. 2006, *AJ*, 131, 168
- Kuehn, F., & Ryden, B. S. 2005, *ApJ*, 634, 1032

- Larson, R. B., Tinsley, B. M., & Caldwell, C. N. 1980, *ApJ*, 237, 692
- Levine, E. S., Schulz, A. E., & White, M. 2002, *ApJ*, 577, 569
- Lidman, C. E., & Peterson, B. A. 1996, *AJ*, 112, 2454
- Lima, M., & Hu, W. 2005, *Phys. Rev. D*, 72, 043006
- Lobo, C., Iovino, A., Lazzati, D., & Chincarini, G. 2000, *A&A*, 360, 896
- Loh, M. et al. 2005, *American Astronomical Society Meeting Abstracts*, 207
- Loh, Y.-S., & Strauss, M. A. 2006, *MNRAS*, 366, 373
- López-Cruz, O., Barkhouse, W. A., & Yee, H. K. C. 2004, *ApJ*, 614, 679
- Lubin, L. M., & Postman, M. 1996, *AJ*, 111, 1795
- Lumsden, S. L., Nichol, R. C., Collins, C. A., & Guzzo, L. 1992, *MNRAS*, 258, 1
- Majumdar, S., & Mohr, J. J. 2003, *ApJ*, 585, 603
- . 2004, *ApJ*, 613, 41
- McKay, T. A., Becker, M. R., Koester, B. P., et al. 2006, in prep.
- McNamara, B. R. et al. 2006, *ArXiv Astrophysics e-prints*
- Merchán, M., & Zandivarez, A. 2002, *MNRAS*, 335, 216
- Miller, C. J. et al. 2005, *AJ*, 130, 968
- Mullis, C. R., Rosati, P., Lamer, G., Böhringer, H., Schwöpe, A., Schuecker, P., & Fassbender, R. 2005, *ApJ*, 623, L85
- Navarro, J. F., Frenk, C. S., & White, S. D. M. 1996, *ApJ*, 462, 563
- Olsen, L. F. et al. 1999, *A&A*, 345, 363
- Popesso, P., Biviano, A., Böhringer, H., & Romaniello, M. 2006, *ArXiv Astrophysics e-prints*
- Popesso, P., Böhringer, H., Romaniello, M., & Voges, W. 2005, *A&A*, 433, 415
- Postman, M., & Geller, M. J. 1984, *ApJ*, 281, 95
- Postman, M., Lubin, L. M., Gunn, J. E., Oke, J. B., Hoessel, J. G., Schneider, D. P., & Christensen, J. A. 1996, *AJ*, 111, 615

- Ramella, M., Geller, M. J., Pisani, A., & da Costa, L. N. 2002, *AJ*, 123, 2976
- Ramella, M. et al. 1999, *A&A*, 342, 1
- Rosati, P., Borgani, S., & Norman, C. 2002, *ARA&A*, 40, 539
- Rozo, E., Wechsler, R. H., Koester, B. P., Evrard, A., & McKay, T. 2006, in prep.
- Ruhl, J., et al. 2004, in *Astronomical Structures and Mechanisms Technology*. Edited by Antebi, Joseph; Lemke, Dietrich. *Proceedings of the SPIE*, Volume 5498, pp. 11-29 (2004)., ed. J. Zmuidzinas, W. S. Holland, & S. Withington, 11–29
- Sandage, A., Binggeli, B., & Tammann, G. A. 1985, *AJ*, 90, 1759
- Sarazin, C. L. 1986, *Reviews of Modern Physics*, 58, 1
- Schwartz, D. A. 1978, *ApJ*, 220, 8
- Sheldon, E. S. et al. 2001, *ApJ*, 554, 881
- Sheldon, E. S., Johnston, D. J., McKay, T. A., Koester, B., et al. 2006, in prep.
- Smail, I., Edge, A. C., Ellis, R. S., & Blandford, R. D. 1998, *MNRAS*, 293, 124
- Stocke, J. T. et al. 1991, *ApJS*, 76, 813
- Stoughton, C., et al. 2002, *AJ*, 123, 485
- Struble, M. F. & Rood, H. J. 1999, *ApJS*, 125, 35
- Tanaka, M., Goto, T., Okamura, S., Shimasaku, K., & Brinkmann, J. 2004, *AJ*, 128, 2677
- The Dark Energy Survey Collaboration. 2005, [arXiv:astro-ph/0510346](https://arxiv.org/abs/astro-ph/0510346)
- Tinker, J. L., Weinberg, D. H., Zheng, Z., & Zehavi, I. 2005, *ApJ*, 631, 41
- Toomre, A., & Toomre, J. 1972, *ApJ*, 178, 623
- Tran, K.-V. H., Simard, L., Zabludoff, A. I., & Mulchaey, J. S. 2001, *ApJ*, 549, 172
- Tucker, D. L. et al. 2000, *ApJS*, 130, 237
- Tully, R. B. 1987, *ApJ*, 321, 280
- van den Bosch, F. C., Mo, H. J., & Yang, X. 2003, *MNRAS*, 345, 923
- Visvanathan, N., & Sandage, A. 1977, *ApJ*, 216, 214

- Voit, G. M. 2005, *Reviews of Modern Physics*, 77, 207
- Wechsler, R. H., Evrard, A. E., McKay, T. A., Koester, B. P., et al. 2006a, in prep.
- Wechsler, R. H., Zentner, A. R., Bullock, J. S., Kravtsov, A. V., & Allgood, B. 2006b, *ApJ*, in press
- Weinmann, S. M., van den Bosch, F. C., Yang, X., & Mo, H. J. 2006, *MNRAS*, 366, 2
- Yang, X., Mo, H. J., van den Bosch, F. C., & Jing, Y. P. 2005, *MNRAS*, 356, 1293
- York, D. G., et al. 2000, *AJ*, 120, 1579
- Zabludoff, A. I., & Mulchaey, J. S. 1998, *ApJ*, 496, 39
- Zwicky, F. 1951, *PASP*, 63, 61
- Zwicky, F., Herzog, E., & Wild, P. 1968, *Catalogue of Galaxies and of Clusters of Galaxies* (Pasadena: California Institute of Technology (CIT), 1961-1968), 0

Table 1. Richness Definitions

Name	Description
M_{200}	Underlying halo mass in mock catalog
N_{int}	Occupation number of halo
N_{int}^{red}	Number of red N_{int} galaxies, brighter than L_{min}
N_{gals}	Number of red galaxies in a cluster, inside h^{-1} Mpc
N_{gals}^{r200}	Number of red galaxies in a cluster, inside r_{200}

Note. — This table is a compilation of the richness measurements used in the halo to cluster comparison in Section 4.

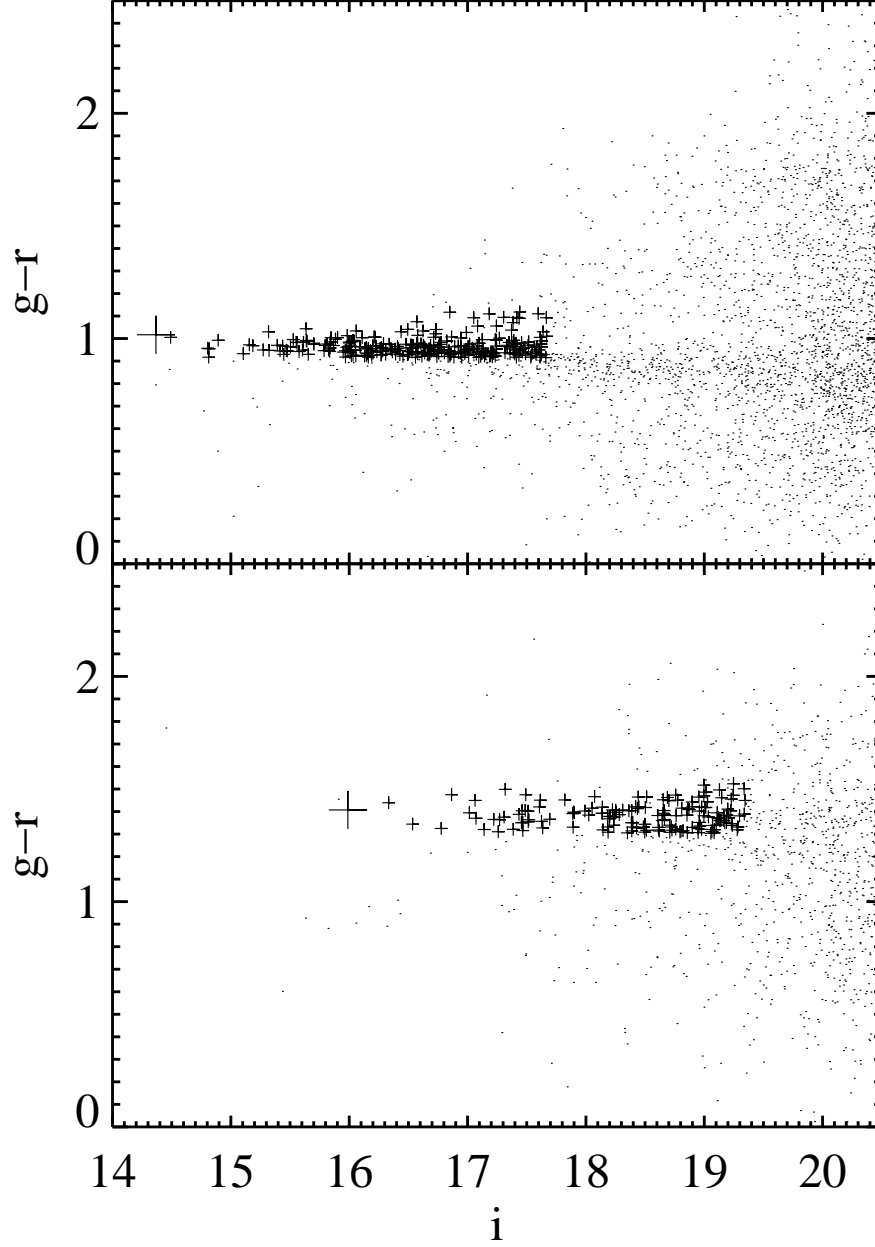


Fig. 1.— BCGs and cluster members in the fields of two rich clusters. The top and bottom plots are the CMDs in the $2h^{-1}$ Mpc surrounding fields of Abell 2142 ($z = 0.092$), and Abell 1682 ($z = 0.23$). The large cross is the BCG, small dots are field galaxies within $2h^{-1}$ Mpc, small crosses are cluster members (see text). The small scatter and tilt in these are clear, particularly in Abell 2142, where the ridgeline can be observed to much fainter magnitudes. Already at $z = 0.23$, we see that the ridgeline is broader, primarily due to photometric errors.

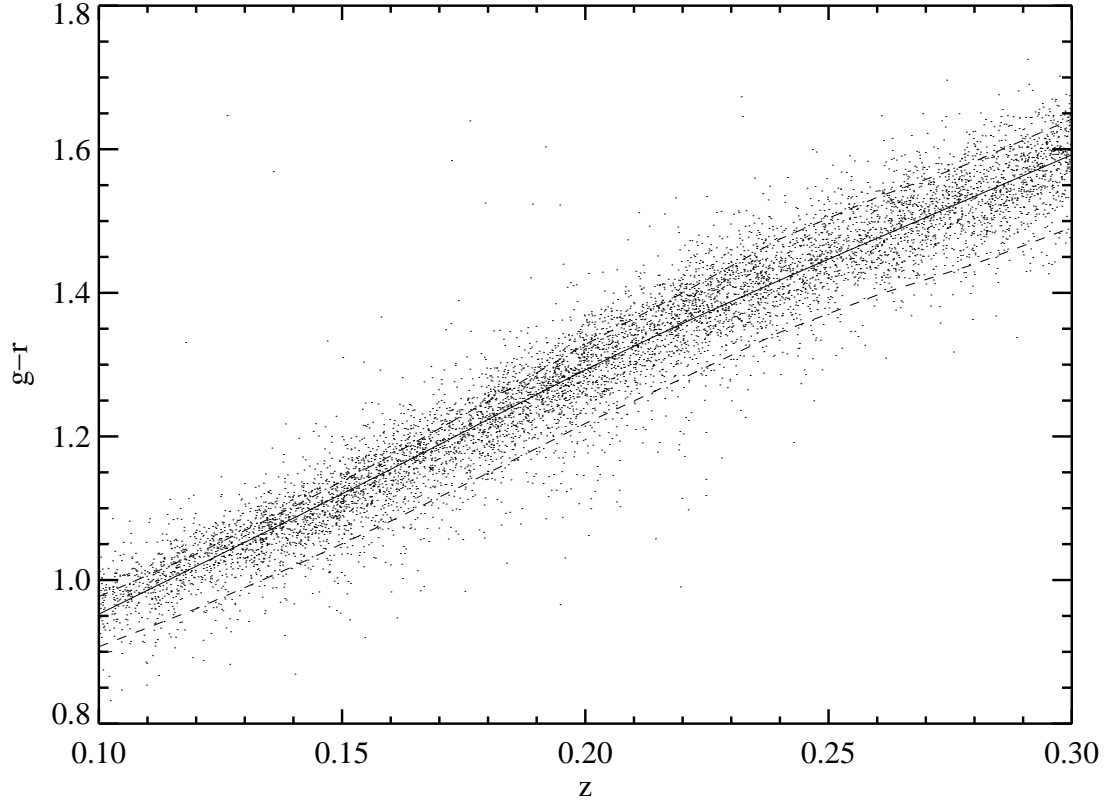


Fig. 2.— Color ($g - r$) vs. spectroscopic z input relation for clusters of all richnesses. Each dot represents cluster members with spectroscopic redshifts. Their color SDSS (MODEL magnitudes) and redshift are plotted. The curve is the piecewise-defined ridgeline-redshift relation, essentially best fits to the cluster colors and redshifts. The upper and lower dotted lines denote the LRG passively-evolving and star-forming colors (see text).

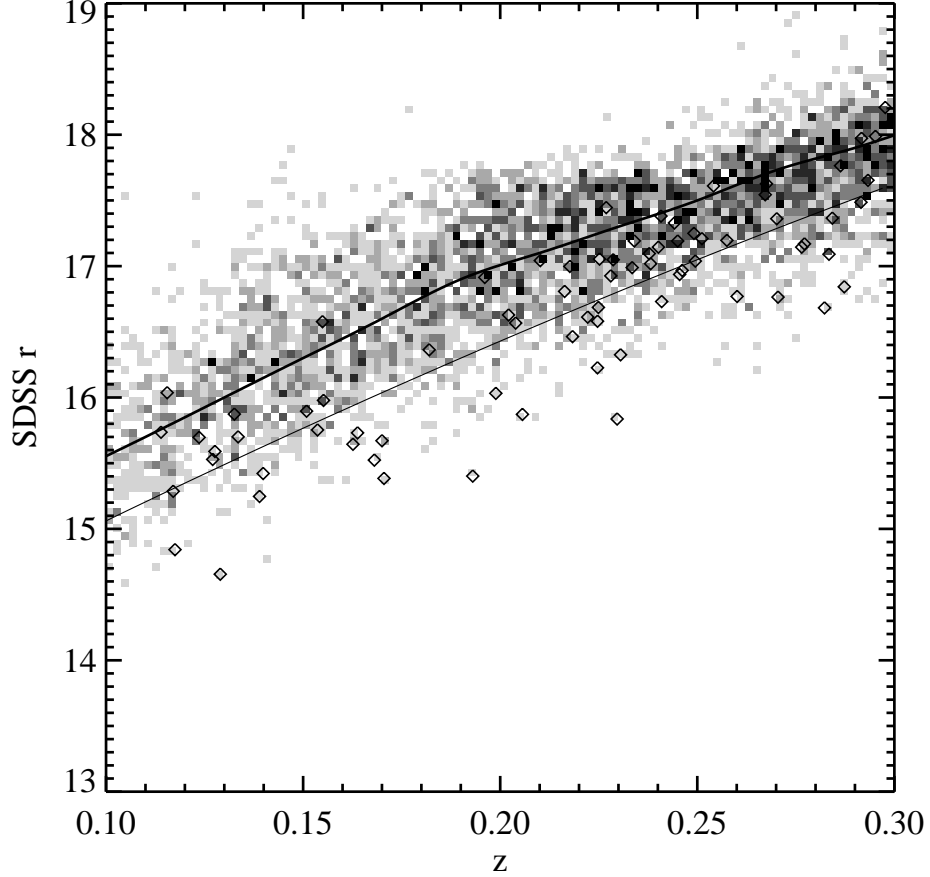


Fig. 3.— Magnitude–redshift relation for BCGs. The upper solid curve is adapted from Loh & Strauss (2006), using r_{petro} . The lower curve is the fit to the r -bands of 100 visually identified BCGs from a first run of maxBCG, diamonds on the plot. Because the magnitudes are observed, distance modulus, k -corrections, and evolution are automatically included. The difference between Loh & Strauss (2006) and this curve is due mainly to the fact that the former do not restrict themselves to the brightest BCGs. The greyscale density plot is the population of BCGs from the maxBCG catalog described in Koester et al. (2006)

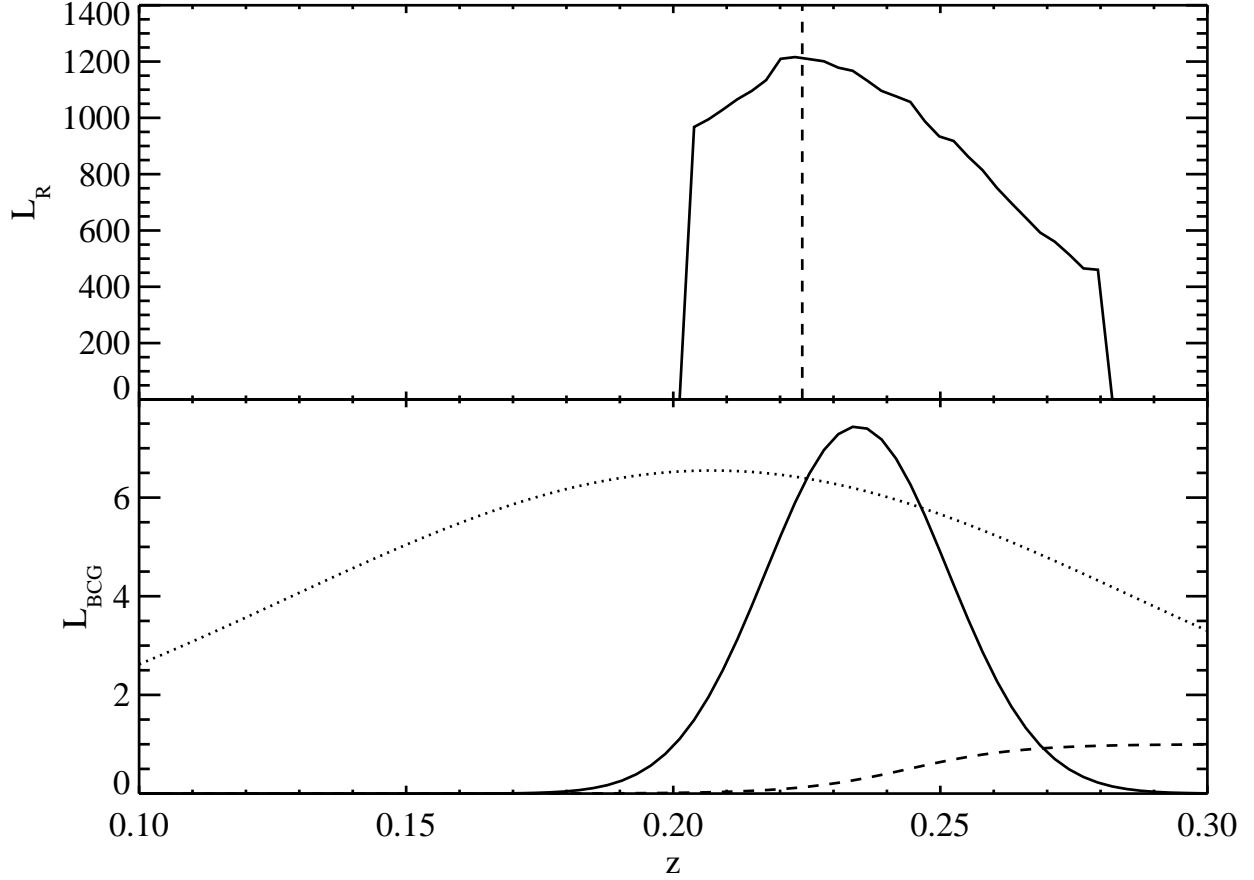


Fig. 4.— Likelihoods for a previously unknown $N_{gals} = 30$, $z = 0.23$ maxBCG cluster. The upper panel shows a sample $\mathcal{L}_R(z)$, with the maximum-likelihood redshift denoted with a vertical line. The components of $\mathcal{L}_{BCG}(z)$ are shown in the lower panel. The narrow Gaussian is G_{gr} , the broad is G_{ri} , and the dashed curve is the magnitude threshold. See the associated image (Figure 6)

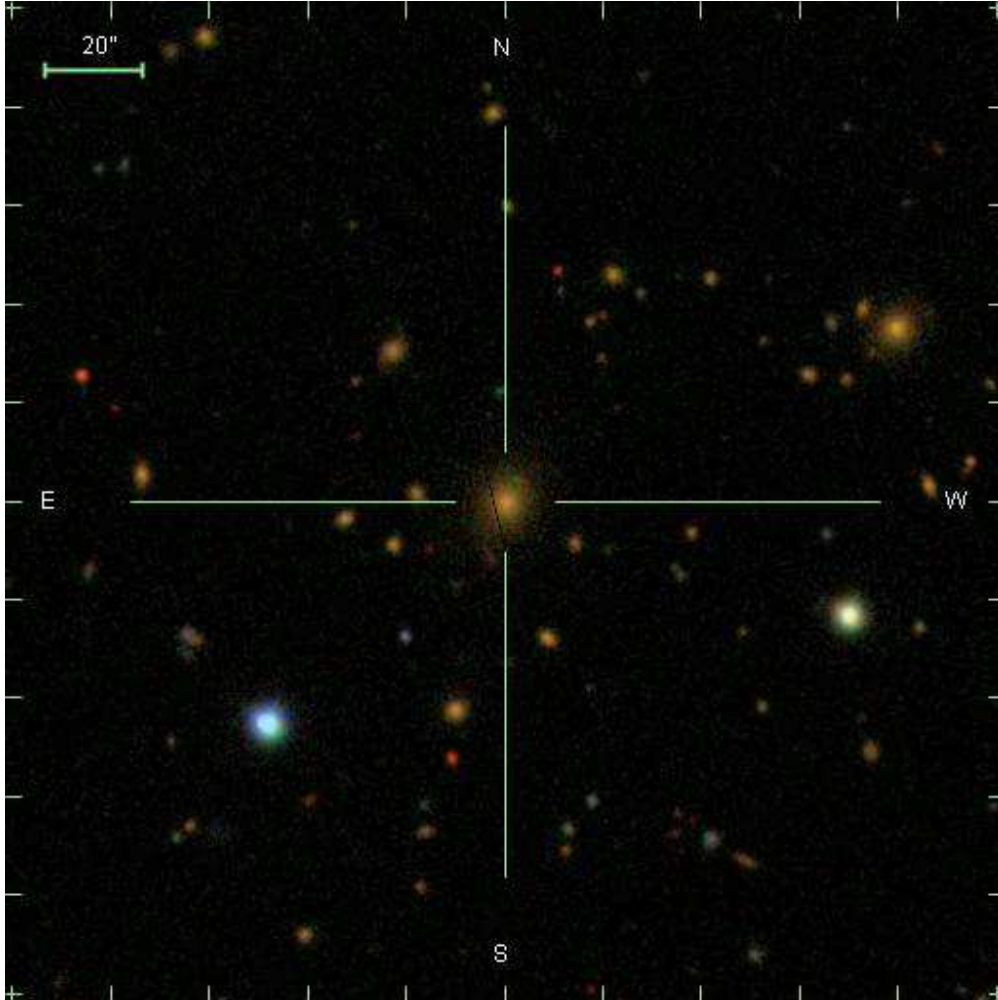


Fig. 5.— Image of object described in text and in Figure 4. Uniform red galaxies dominate the image, which spans $200''$, or $\simeq 0.5h^{-1}$ Mpc. See online edition of the Journal for color image.

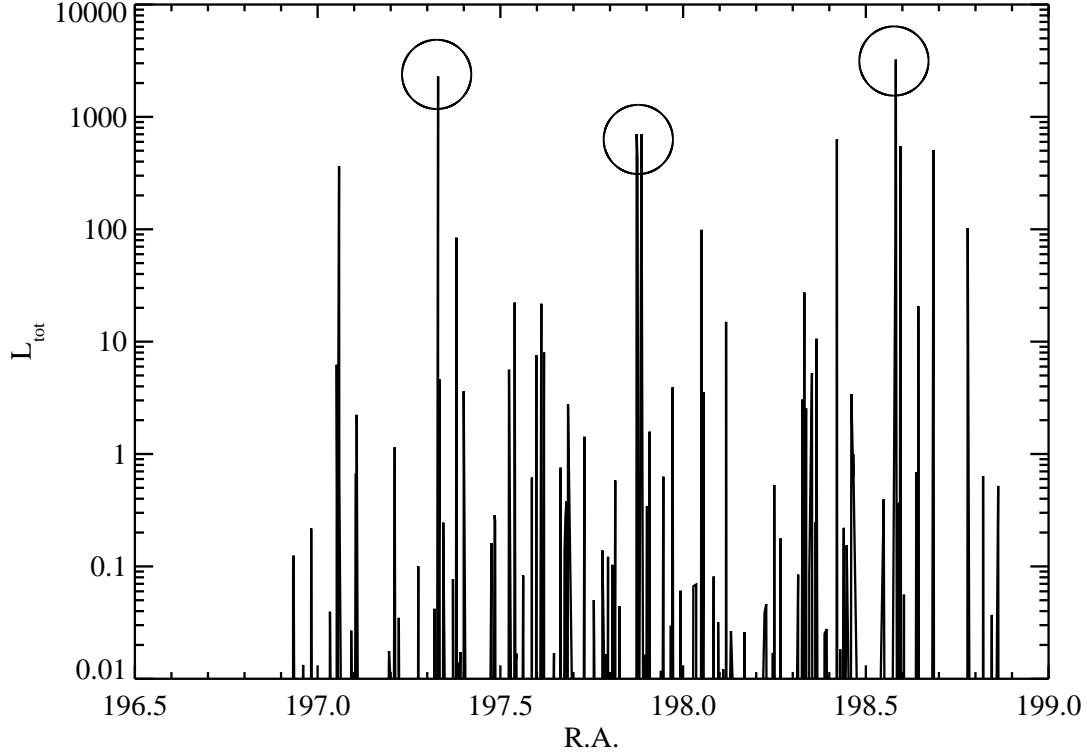


Fig. 6.— Cluster likelihoods in the field of Abell 1689 (center circle). Two other high likelihood peaks also reside in this field. At (197.33,-1.62), $z = 0.08$, is a REFLEX X-ray selected cluster, MS 1306.7-0121 (left circle, Böhringer et al. 2004). At (198.58,-1.46), $z = 0.18$, is NSC J131423-012734, part of the Northern Sky Optical Cluster Survey (Gal et al. 2003).

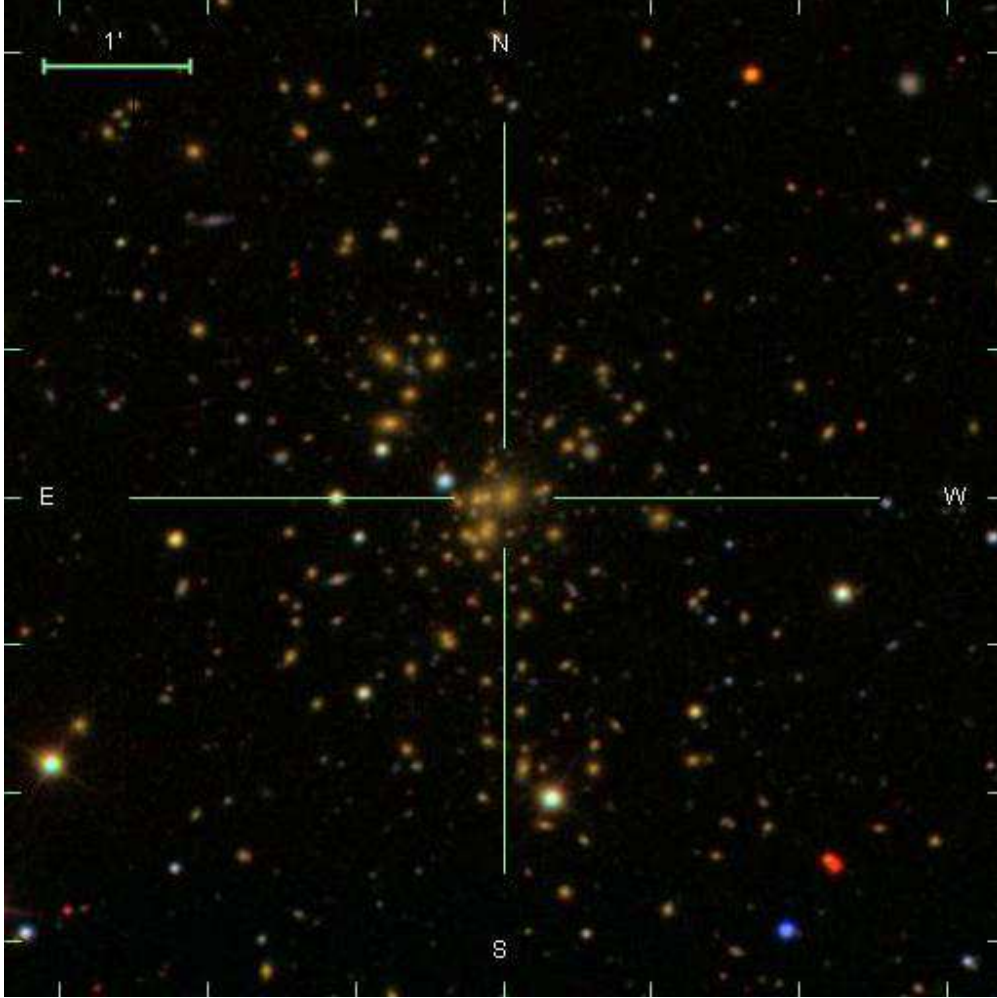


Fig. 7.— Abell 1689, positioned on the maxBCG center. The FOV is $\simeq 0.75h^{-1}$ Mpc wide. The image is overwhelmed with luminous red cluster galaxies, essentially all at the same redshift. In Abell et al. (1989), the position given is (ra,dec)=(197.8917,-1.365), which is 0.03 degrees different from the maxBCG position, or $\simeq 230$ kpc. The redshift given by Struble & Rood (1999) is $z = 0.1832$, compared to $z = 0.189$ given by maxBCG. Also, note that the colors of these are less red than those from Figure 5, the $z = 0.23$ cluster. See online edition of Journal for color image version.

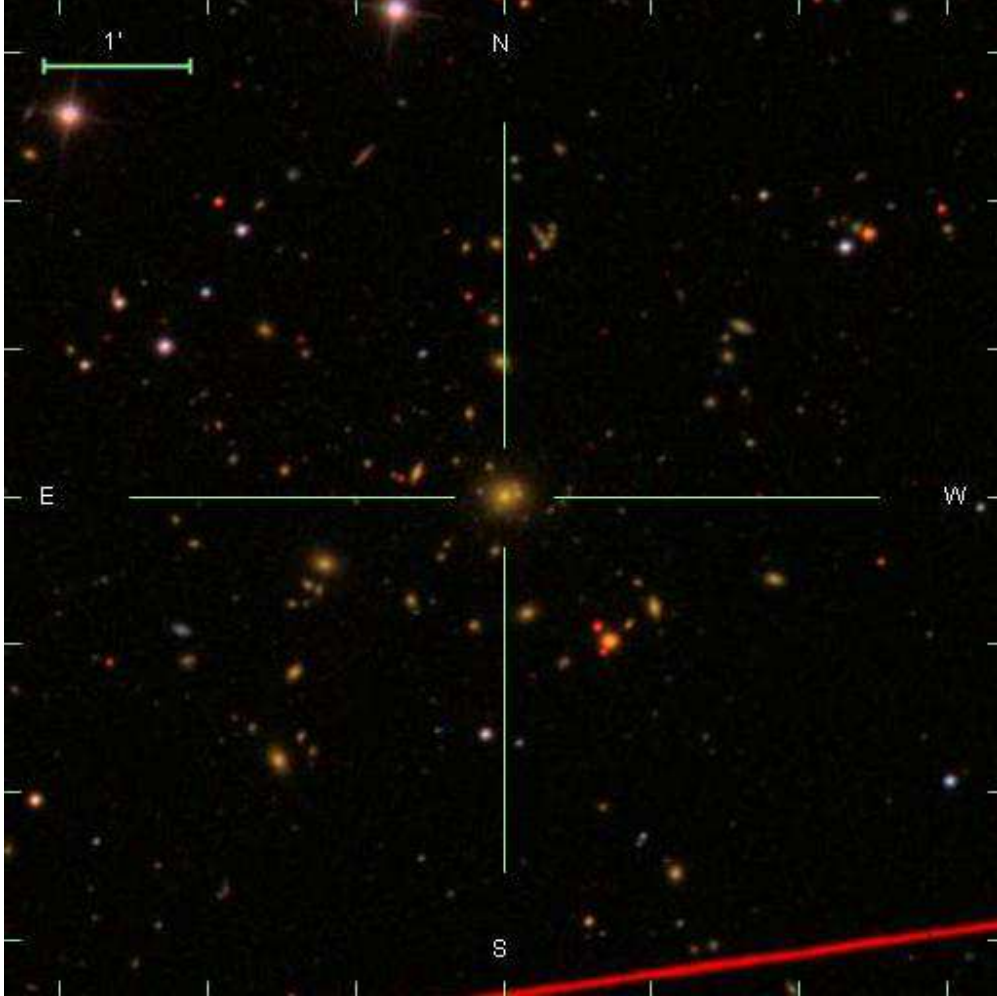


Fig. 8.— NSC J131423-012734, at $z=0.18$ in the field of Abell 1689, ~ 0.75 degrees away. The FOV is also $\simeq 0.75h^{-1}$ Mpc, centered on the maxBCG position. The NSC catalog (Gal et al. 2003) quotes a position at (ra,dec)=(198.5983,-1.4597), 0.016 degrees from the maxBCG center, or $\simeq 125$ kpc. The NSC photometric redshift of $z = 0.247$ is not consistent with maxBCG, which gives $z = 0.181$. SDSS spectroscopy provides redshifts for 4 cluster members, all at nearly $z = 0.18$. See online edition of Journal for color image.

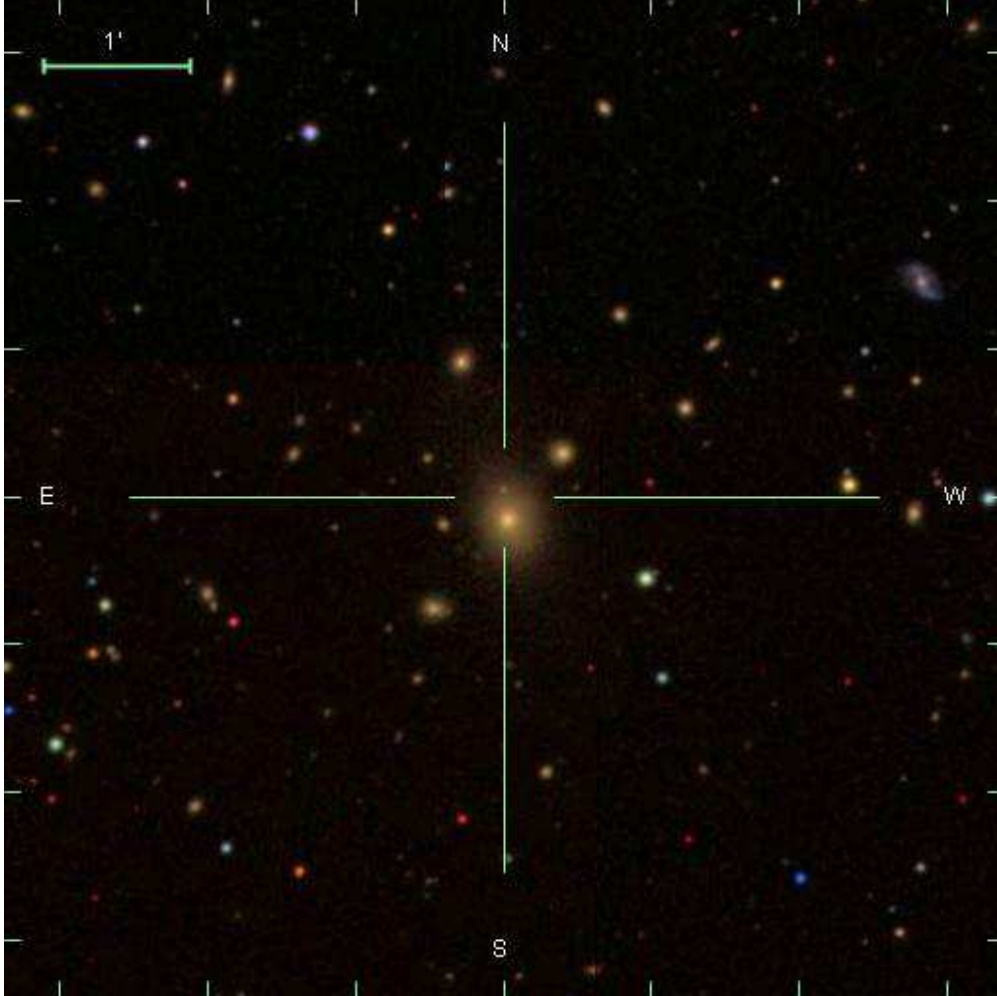


Fig. 9.— MS 1306.7-0121, an X-ray selected cluster at $z = 0.08$, in a FOV spanning $\simeq 0.38h^{-1}$ Mpc. In Stocke et al. (1991), the position is given as (ra,dec)=(197.3254,-1.6228), 0.005 degrees from the maxBCG center, or $\simeq 20$ kpc. Its redshift is $z = 0.088$, compared to the $z = 0.08$ given by maxBCG. The BCG is clearly dominant and the colors of this lower redshift cluster are slightly less red than the previous two images, and quite noticeably bluer than Figure 5. See online edition of Journal for color image.

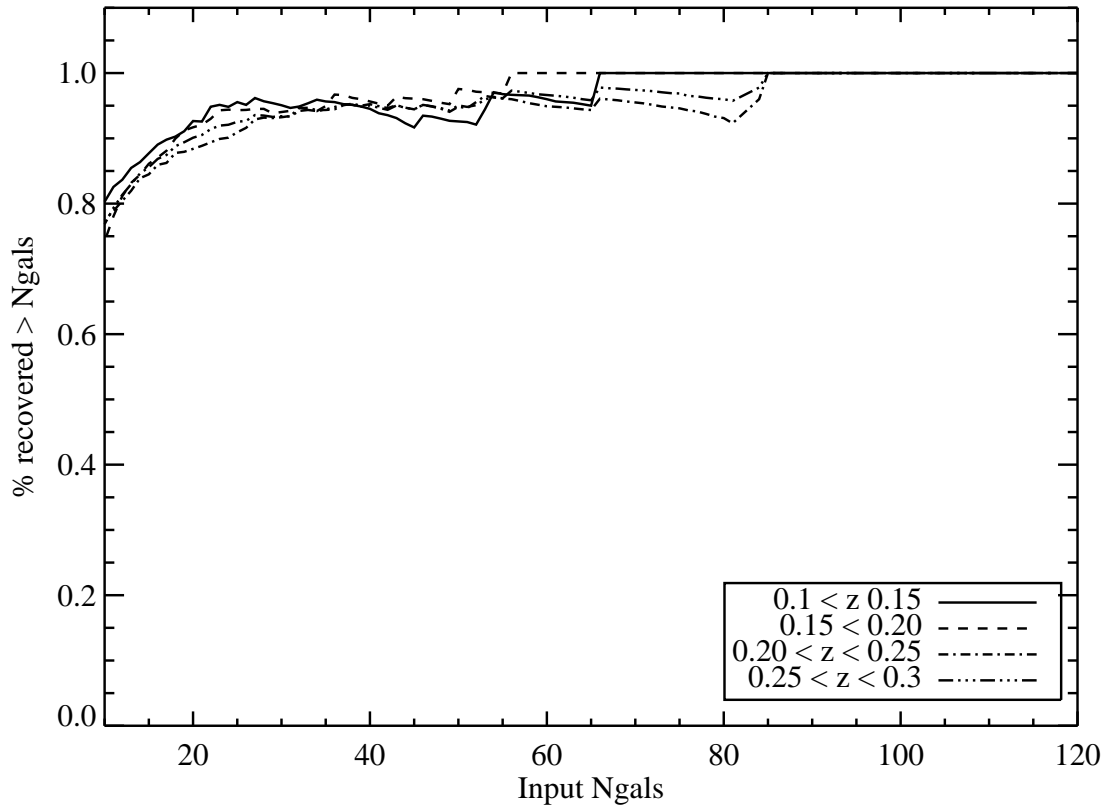


Fig. 10.— Monte-Carlo Completeness of MaxBCG. The completeness is tested using shuffled catalogs with artificial clusters similar to Goto et al. (2002) (see text).

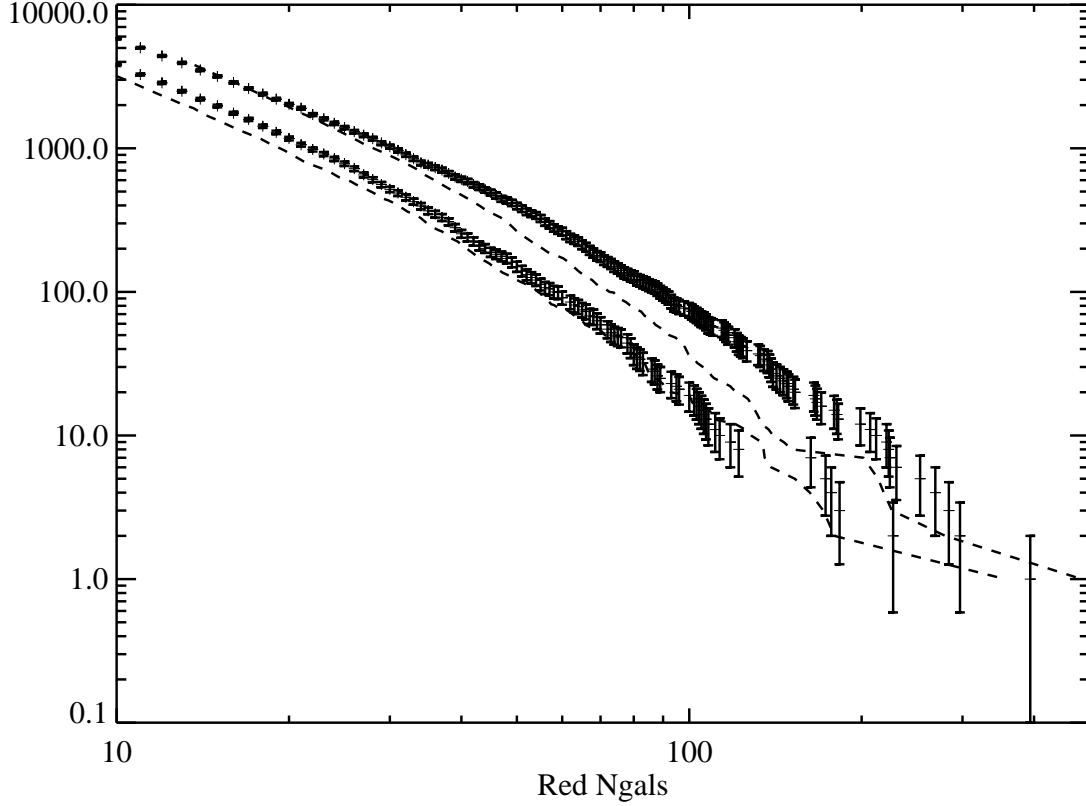


Fig. 11.— Integrated counts for the derived cluster catalog (upper points, N_{gals}^{r200}) compared to the halo abundances, using N_{int}^{red} as the halo richness. Poisson error bars are overplotted. The offset stems from richness estimates (§4.2) and fragmentation and overmerging (§4.3). In §4.2, a richness correction is determined by the simplest halo to cluster matching scheme. Assuming the differences are due only to richness estimation, the correction is applied to each abundance. The upper dotted line gives the new halo abundance after correction of the halo richnesses, and the new cluster abundance, where cluster richnesses are corrected, is given as the lower dotted line. Clearly, the process is not commutative.

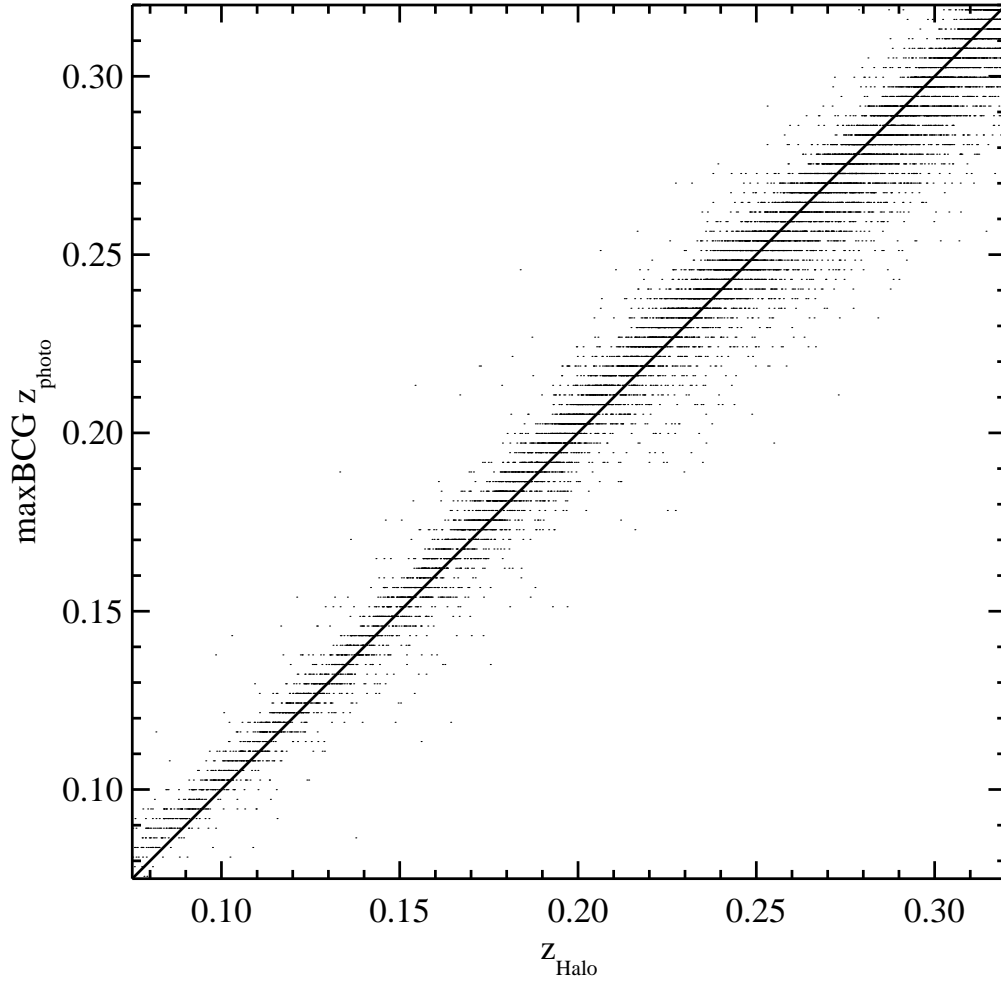


Fig. 12.— Accuracy of the photometric redshift estimation for clusters. Plot compares the redshift identified for maxBCG clusters in the mock catalog with the redshift of the best-matched dark matter halo.

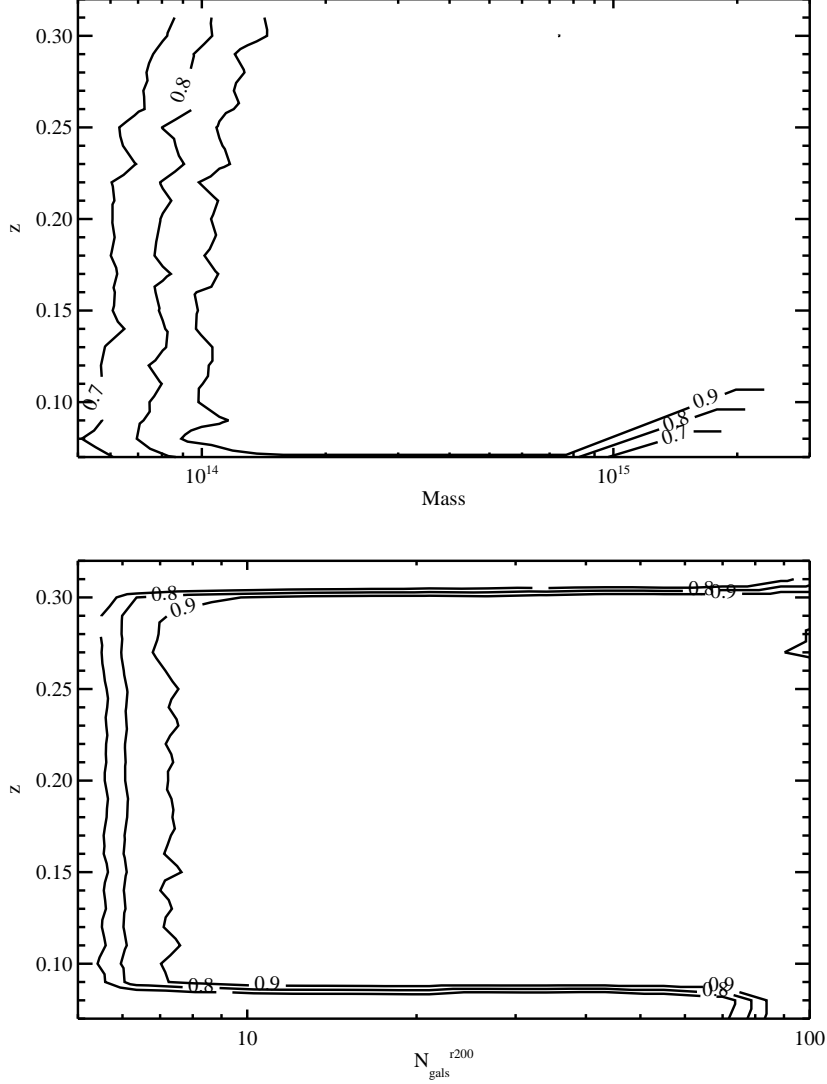


Fig. 13.— Completeness and purity. The top panel shows contours of constant completeness in the redshift-mass plane, for a matching fraction of $f_h = 0.3$. The lower panel shows contours of constant purity in the redshift $N_{\text{gals}}^{r200} - z$ plane, for a matching fraction of $f_c = 0.3$. The decrease in completeness at low mass, and purity at low and high redshift are due to the chosen cuts on cluster richness and redshift: lower mass halos are found, but have < 10 red galaxies, and clusters at the redshift boundaries are often associated with halos just outside $z = 0.1$ or $z = 0.3$.

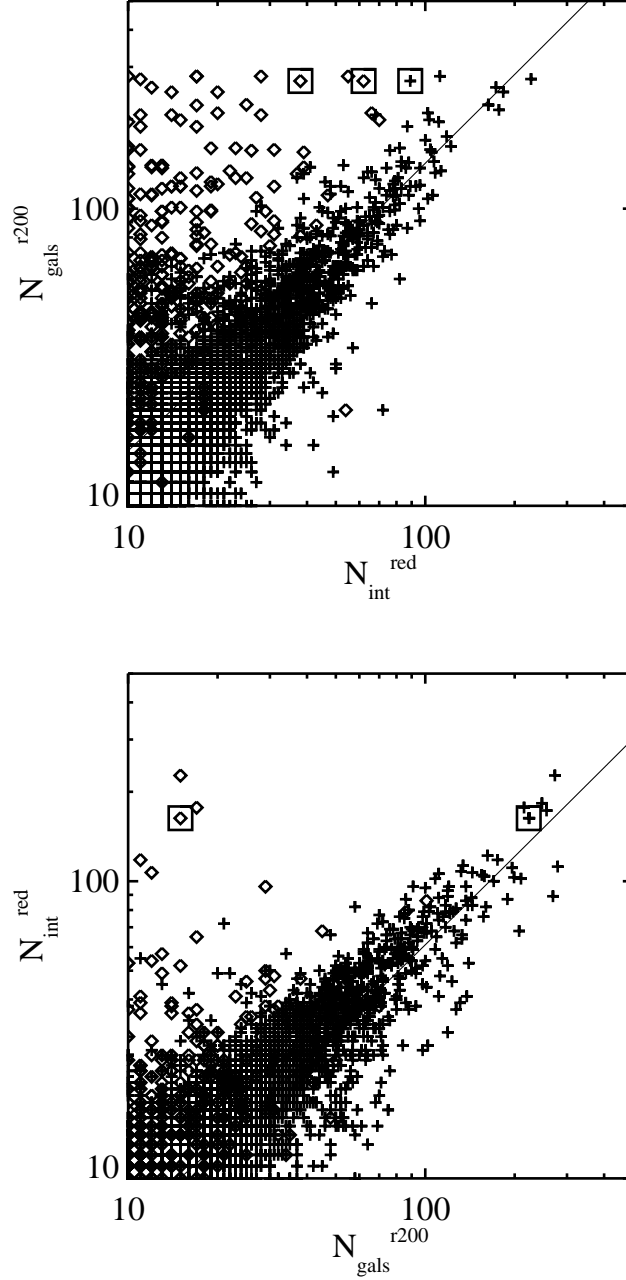


Fig. 14.— Richness scalings between cluster and halo catalogs. *Top Panel*: Halos matched to clusters. For each halo $N_{\text{gals}}^{\text{red}}$ is plotted vs. N_{gals}^{r200} of the best-matched cluster. The diamonds represent duplicate halos (see text), and boxed points are examples cited in the text. *Bottom Panel*: Clusters are matched to halos. For each cluster N_{gals}^{r200} is plotted vs. $N_{\text{gals}}^{\text{red}}$ of the best-matched halo. The diamonds represent duplicate clusters (see text). Solid lines represent the mean relations in each case.

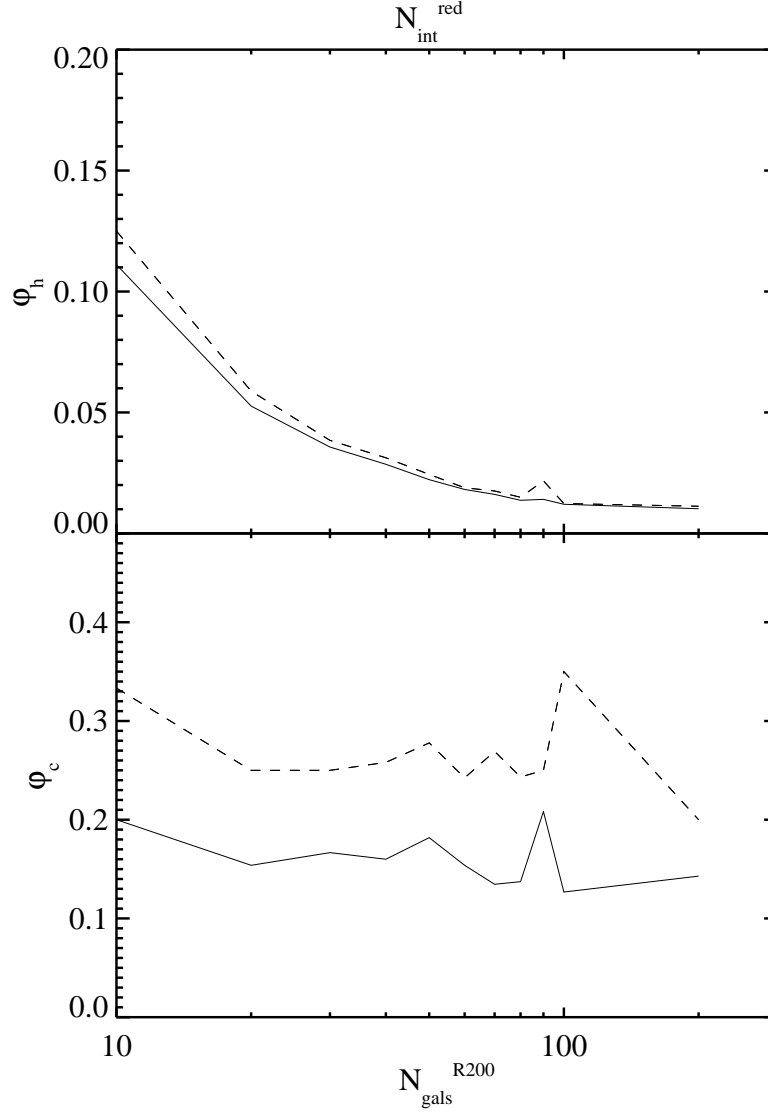


Fig. 15.— Fragmentation and overmerging as a function of richness. Upper panel shows fragmentation of halos, as a function of their red-galaxy richness (as defined by Eq. 14); lower panel shows the overmerging of halos, as a function of cluster ridgeline richness. The solid lines in upper and lower panels display the median amount of fragmentation and overmerging, respectively, while the dotted lines indicate the first quartile of the respective distribution. Fragmentation is nearly non-existent, while small-scale projection along the line of sight causes slight overmerging that boosts the cluster richness estimates by 10–20 percent.

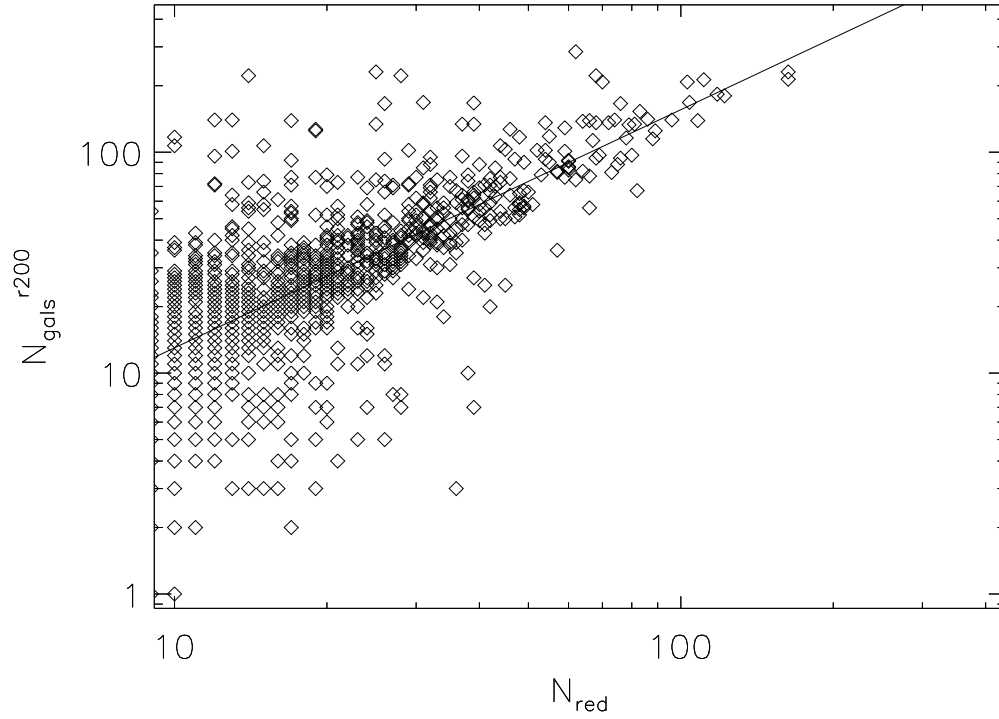


Fig. 16.— Exclusive matching of clusters and halos, adapted from Rozo et al. (2006). A full account of the algorithmic properties presented in section 4 enables a well-defined matching of halos and clusters, as presented in Rozo et al. (2006). This is clearly a marked improvement on the upper panel of Figure 14, and demonstrates the efficacy of an exclusive matching algorithm.

This figure "f5.jpg" is available in "jpg" format from:

<http://arxiv.org/ps/astro-ph/0701268v1>

This figure "f7.jpg" is available in "jpg" format from:

<http://arxiv.org/ps/astro-ph/0701268v1>

This figure "f8.jpg" is available in "jpg" format from:

<http://arxiv.org/ps/astro-ph/0701268v1>

This figure "f9.jpg" is available in "jpg" format from:

<http://arxiv.org/ps/astro-ph/0701268v1>